André Alves Silva

Licenciado em Ciências de Engenharia Mecânica

# Dynamic Analysis of Numerical Mesoscale Models of Composite Materials

Dissertação para obtenção do Grau de Mestre em Engenharia Mecânica

Orientadora: Professora Doutora Marta Isabel Pimenta Verdete da Silva Carvalho, Professora Auxiliar Convidada da Faculdade de Ciências e Tecnologia da Universidade Nova de Lisboa

Co-Orientador: Doutor Pedro Miguel de Almeida Talaia, Engenheiro de I&D, CEiiA

Júri:

| | |
|---|---|
| Presidente: | Doutor Pedro Samuel Gonçalves Coelho |
| Arguente: | Doutor João Mário Burguete Botelho Cardoso |
| Arguente: | Doutor Bernardo Rodrigues de Sousa Ribeiro |
| Vogal: | Doutor Pedro Miguel de Almeida Talaia |

FACULDADE DE CIÊNCIAS E TECNOLOGIA
UNIVERSIDADE NOVA DE LISBOA

Setembro 2016

**Dynamic Analysis of Numerical Mesoscale Models of Composite Materials**

*To my family*

# Acknowledgements

To Assistent Professor Marta Carvalho, supervisor of this dissertation, for her availability to help me, and the patience and encouragement provided in the most difficult times. For all she taught me, even in times I was more nervous she always helped me.

To Assistent Professor João Cardoso, for all he taught me throughout my academic life and for his availability to help me in times of need.

To Faculdade de Ciências e Tecnologia at Universidade Nova de Lisboa and CEiiA for the opportunity to develop this dissertation, and more particularly, to Dr. Pedro Miguel de Almeida Talaia for all the advices he gave me, even in the most occupied times.

To all the professors of the Department of Mechanical and Industrial Engineering, for all their contribution to my academic career.

To my family, who never stopped supporting and helping me. To my mother and my father, my pillars, who helped me in the moments I needed the most.

To Dr. Carla Machado for all the support and help she gave me.

To Tiago, Filipe and my friends, who stood by me this last five years, for all the crazy moments, for, sometimes, testing my patience, but most of all for all the companionship, friendship and support. To Pedro Mangualde, one of my lab partners, for the help and for the humorous conversations that made working easier and to Ricardo Marchão, one of the most honest people I met and, also, as nervous as me, for all the friendship and support over this last few years.

# Abstract

The role of composites in the industry has been increasing over the past few years. One of the main reasons for this phenomenon is due to these materials presenting the best properties of their constituents and often qualities that neither of the constituent materials have. However, as a consequence, composite structures are becoming more complex, and its behavior more difficult to predict.

The study of this dissertation arises from Crespo's dissertation, and had its origin on the need to predict the behavior of composite materials specimens in a less expensive and faster manner. To fulfill this need, a methodology was developed using LS-DYNA finite element mesoscale models.

This methodology uses an explicit dynamic analysis, and is capable of testing composite specimen models subjected to tensile and compressive loads. However, this type of analysis is different from the one Crespo used and phenomenons like hourglass must be considered. For this case study the material model consists in a spread tow carbon fabric with 0°/90°, 15°/75° and 30°/60° arrangements. To simulate the behavior of this composite material, when subjected to external loads, failure and damage propagation such as delamination, fiber and matrix failure are implemented in the models. The failure of the matrix and the fibers are controlled by a combined failure criterion implemented in LS-DYNA code.

Knowing only the dimensions of the test specimens, the material properties were taken from Crespo's dissertation. To validate the models, results were compared with Mangualde's, whose methodology was developed using an implicit static analysis.

Keywords: delamination, hourglass, failure criterion, explicit dynamic analysis, mesoscale

# Resumo

O papel dos materiais compósitos na indústria tem vindo a aumentar ao longo dos últimos anos. Uma das principais razões para este fenómeno deve-se ao facto destes materiais apresentarem propriedades superiores ao dos seus constituintes e, na maior parte das vezes, qualidades que nenhum dos materiais constituintes tem. No entanto, como consequência, as estruturas de compósitos são cada vez mais complexas e o seu comportamento cada vez mais difícil de prever.

O estudo feito nesta dissertação surge no âmbito da dissertação da Inês Crespo, e teve a sua origem na necessidade de prever o comportamento de provetes de materiais compósitos de uma forma menos dispendiosa e mais rápida. A fim de cumprir esta necessidade, foi desenvolvida uma metodologia com recurso a modelos à meso-escala de elementos finitos utilizando o LS-DYNA.

Esta metodologia utiliza uma análise dinâmica explícita e é capaz de testar modelos de amostras de compósitos submetidos a cargas de tração ou compressão. No entanto, este tipo de análise é diferente da que a Inês Crespo utilizou e fenómenos como o *hourglass* têm de ser considerados. Para este estudo o material consiste num tecido ultrafino de carbono com fibras orientadas a 0°/90°, 15°/75° e 30°/60°. De forma a simular o comportamento deste material quando submetido a cargas externas, foram implementados mecanismos de falha e propagação de dano no modelo, tais como delaminação e falha das fibras e da matriz. Estas últimas são controladas por uma combinação de dois critérios de falha que se encontram implementados no código do LS-DYNA.

As propriedades dos materiais foram obtidas do modelo numérico da dissertação de Inês Crespo, conhecendo-se apenas as dimensões dos provetes. De forma a validar a metodologia, os resultados apresentados nesta dissertação foram comparados com os resultados obtidos por Pedro Mangualde, cuja metodologia foi desenvolvida recorrendo a uma análise estática implícita.

Palavras-Chave: delaminação, *hourglass*, critério de falha, análise dinâmica explícita, meso-escala

# Table of Contents

# List of Figures

# List of Tables

# Nomenclature and List of Symbols

| | |
|---|---|
| CFRP | Carbon Fiber Reinforced Polymer |
| RTM | Resin transfer molding |
| SRIM | Structural reaction injection molding |
| RFI | Resin film infusion |
| FEM | Finite element method |
| RVE | Representative volume element |
| HG | Hourglass |
| S/R | Selectively reduced |
| CPE | Cosserat Point Element |
| IFT | Interlaminar fracture toughness |
| VCCT | Virtual crack closure technique |
| TBI | Tie-Break interface |
| CZM | Cohesive zone model |
| DCB | Double cantilever beam |
| $\sigma$ | Stress |
| $\varepsilon$ | Strain |
| $E_i$ | *Young's moduli* for the *i*-direction |
| $v_{ij}$ | Poisson's ratio |
| $G_{ij}$ | *Shear moduli* for the plane ij |
| $X_T$ | Failure stress under longitudinal tension |
| $X_C$ | Failure stress under longitudinal compression |
| $Y_T$ | Failure stress under transversal tension |
| $Y_C$ | Failure stress under transversal compression |
| $S_L$ | Failure stress under pure shear |
| $\alpha$ | Fracture angle |
| $\varepsilon_{iT}^{u}$ | Tensile normal failure strain |
| $\varepsilon_{iC}^{u}$ | Compressive normal failure strain |
| $\varepsilon_{ijT}^{u}$ | Shear strain failure in the plane ij |
| $F_{ij}$ | Variables implemented in the Tsai-Wu failure criterion |
| $T$ | Total potential energy |

| | |
|---|---|
| $\pi$ | Kinetic energy |
| $u$ | displacement |
| $\dot{u}$ | Velocity |
| $M_{JK}$ | Mass matrix |
| $C_{JK}$ | Damping matrix |
| $K_{JK}$ | Stiffness matrix |
| $\bar{u}_k$ | Amplitude of the sinusoidal vibration |
| $w$ | Natural frequency |
| $G_{IC}$ | Critical energy for Mode I |
| $G_{IIC}$ | Critical energy for Mode II |
| $G_{IIIC}$ | Critical energy for Mode III |
| $EN$ | Stiffness normal to the plane of the cohesive element |
| $ET$ | Stiffness in the plane of the cohesive element |
| $\delta_m$ | Mixed-mode relative displacement |
| $\delta_I$ | Separation in the normal direction for Mode I |
| $\delta_{II}$ | Separation in the transverse direction for Mode II |
| XMU | Exponent of the mixed mode criteria |
| $\delta_F$ | The ultimate mixed-mode displacement |
| $\beta$ | "mode mixity" |
| $W$ | Width |
| $L$ | Length |
| $t$ | Thickness |
| $T$[1] | Peak traction in the normal direction |
| $S$ | Peak traction in the tangential direction |
| $K$ | Interface stiffness |
| $UND$ | The ultimate displacement in the normal direction |

[1] Variable displayed from Chapter 4

# 1 Introduction

## 1.1 Motivation

Composites materials have existed for a long time, however their importance has been increasing over the past few years. In the automobile, aeronautic and naval industry the use of these materials is becoming higher, replacing the use of traditional materials. As a consequence, the requirements are becoming more specific and the composite structures more complex. For this reason, it is very important and a priority for an engineer the knowledge and comprehension of the characteristics and behavior of these materials.

As technology evolves, new ways of producing composites are being developed. Currently, carbon fiber reinforced polymer (CFRP) is a new composite material that is being introduced in the industry. The properties and behavior of this composite are acquired by very expensive tests using the Building Block approach [1]. These new materials can be characterized by their matrix, which can be, for example, an epoxy resin, their reinforcement material and stacking sequence (number, thickness and fiber orientation). It is important to note that a single change in the characteristics of these materials would imply a repetition of the tests previously submitted.

The present dissertation follows on Crespo's dissertation [2], that developed numerical mesoscale models for static analysis of composite materials in order to study its collapse when subjected to uniaxial compression tests. Some factors were identified in order to improve the work that Crespo developed, including the computational cost and parameter identification using optimization methodologies. With this under consideration, it was proposed the development of numerical models for dynamic analysis that, not completely replacing the experimental tests that are already implemented, allows the user to acquirer most of the knowledge of the behavior of the tested material in a simpler and less expensive way with the objective of increasing and speeding the accessibility of these materials in the industry

## 1.2 Objectives

As previously stated, nowadays the knowledge of composite material structures are acquired using the Building Block approach, which will be described further ahead. However, the cost and time inherent to this approach becomes counter-productive. Due to that, the development of numerical models is becoming an increasingly important tool, allowing most of the knowledge to be acquired in a faster and less expensive way.

In this dissertation, in order to develop a numerical model for predicting composite material behavior capable of providing accurate results it is required to establish objectives. The main objective of this dissertation is to develop numerical mesoscale models for explicit dynamic analysis with different arrangements using LS-DYNA [3] and respectively validate them with Mangualde's models [4], whose dissertation was developed in the same semester, and the results obtained from experimental tests. In Figure 1.1 an example of experimental results obtained from testing test specimens constituted by 26 plies subjected to compressive loads is represented as well as an organizational chart describing the work that will be developed in a structured way.

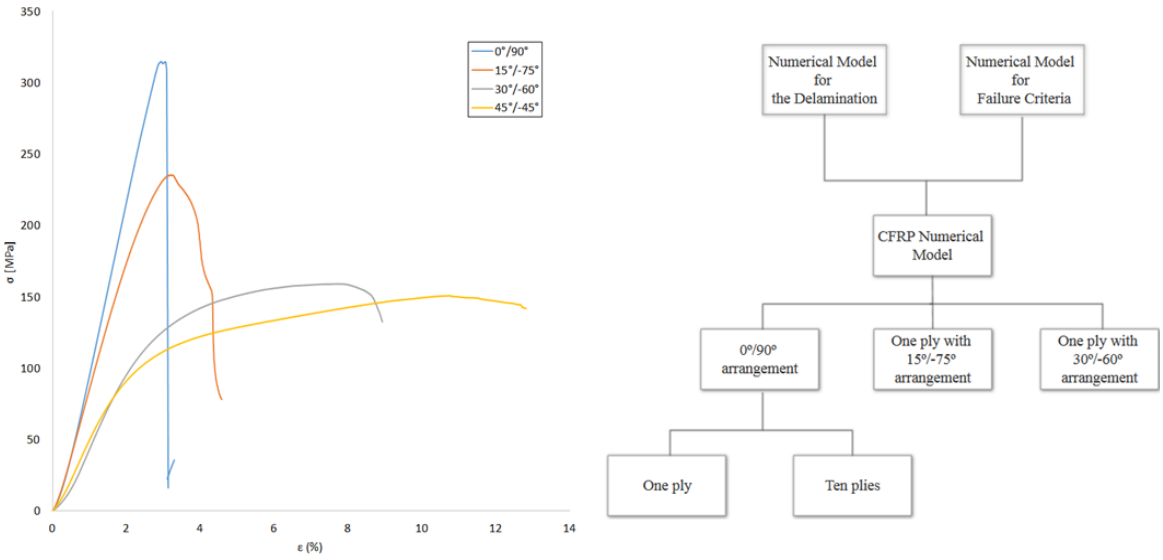


**Figure 1.1-** Experimental results of a test specimen constituted by 26 plies with four different orientations and an organizational chart describing the work developed

## 1.3 Structure

The work that was developed and described in the present dissertation is divided in five chapters, being this chapter the first, where the motivation, objectives and the respective structure are described.

In Chapter 2 is presented the state of the art, where the theoretical concepts are described. In this chapter, most of the work and studies that have been done related to composite materials, multiscale modes, failure modes, failure criteria and dynamic analysis, among other relevant subjects, are presented.

In Chapter 3 a detailed review of delamination, the combined failure criteria and their respective implementations in the LS-DYNA code are presented. The respective models are then described and simulated, comparing the results with the ones obtained by Mangualde's simulation, and respectively validated.

Chapter 4 is presented as the final chapter of results, where ten numerical modes, six models of one ply with a 0°/90°, 15°/-75° and 30°/-60° arrangement, with and without cohesive contact and two models for ten and twenty-six plies with a 0°/90° arrangement are tested implementing all the features described in the previous chapters. The results are then compared with the results obtained by Mangualde and Crespo's simulation.

Finally, in chapter five all the conclusions obtained during all the work that was developed throughout this dissertation are presented, as well as a review of the objectives that were proposed in the beginning. In the last subject of this chapter, ideas and improvements are suggested in order to follow all the work that was developed.

# 2
# Theoretical Framework

## 2.1 Concepts of Composite Materials

A composite material can be defined as a combination of two or more distinct materials in a macroscopic structural unit, having a recognizable interface between them [2,5].

Given the information in the ASM Handbook Vol. 21 [1], composites are commonly classified at two distinct levels. The first level refers to the matrix constituent, in which these materials act as a binder for the reinforcements, transferring the loads between and protecting them from the environment. The second level refers to the reinforcement constituent. It is the reinforcement which gives the composite its desired properties. Composites can also be classified by a continuous phase (the matrix) and a discontinuous phase (the reinforcement). As stated by George H. Staab [6] the constituents are generally arranged so that one or more discontinuous phases are embedded in a continuous phase.

The resulting composite has a superior balance of structural properties comparing to either constituent material alone. This balance and, as a consequence, improved structural properties, result from a load-sharing mechanism.

A material is generally stronger and stiffer in fiber form than in bulk form. Individual fibers are harder to control and arrange in usable components. Therefore a binder material (the matrix) is required and must be continuous in order to surround each fiber so that they are kept distinctly separate from adjacent fibers, allowing the entire material system to be easier to handle and work with [6].

According to Music and Witdroth [7], the constituents remain separate and are easily distinguishable, making the material heterogeneous. Thus, the overall properties of a composite part depend on the properties of both components, the interface between them and the methods used to manufacture it.

The main advantage of these materials is that they usually present the best properties of their constituents and often qualities that neither of the constituent materials have [2]. Some of the properties that can be improved by producing a composite material are strength, stiffness, corrosion resistance, wear resistance, weight, fatigue life, temperature-dependent behavior, thermal insulation, thermal conductivity or acoustical isolation [2].

### 2.1.1 Reinforcement

As previously stated, the reinforced constituent is the component that provides the desired properties to the final product (the composite material), whether it's strength, stiffness or both. These constituents can be classified in three different ways: particulate, continuous and discontinuous fibers, as represented in Figure 2.1. Reinforcement is considered to be a "particle" if all of its dimensions are roughly equal [1].

According to Music and Witdroth [7], when using short fiber (particulate or discontinuous) it's required that the matrix transfers the load between the reinforcement more frequently, resulting in a composite with low properties when compared with a composite that is reinforced with continuous fibers.

The first composites ever produced were the fiberglass-reinforced plastics, which are sometimes referred to as "basic" composites, but nowadays the most widely used are the advanced fibers, such as carbon and graphite fibers [5]. The advantages of these fibers, when compared with glass fibers, are their higher modulus and lower density.

The reinforcement material of the specimens studied in this dissertation is Carbon Fiber.

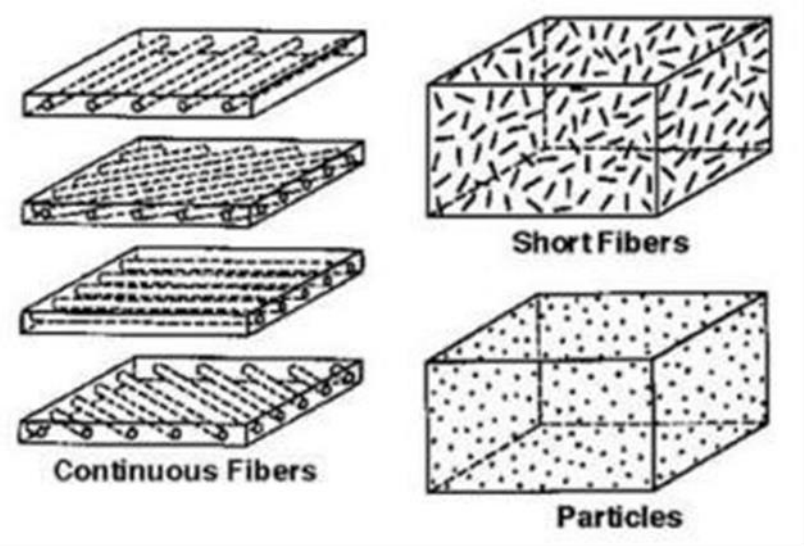


**Figure 2.1-**Different types of reinforcements [7]

### 2.1.2 Matrix

The matrix constituents can be polymers, metals or ceramics, depending on the particular requirements [5]. It's the matrix that holds the fibers together in a structural unit, due to their cohesive and adhesive characteristics, protecting them from external damage, as well as transferring and distributing the applied loads to the fiber, allowing the strength of the reinforcements to be used to their full potential [3,1]. It also provides a solid form to the composite in order to facilitate handling during manufacture. As previously stated the reinforcements are stronger and stiffer than the matrix. Therefore, as a continuous phase, the matrix controls the transverse properties, interlaminar strength and elevated-temperature strength of the composite.

Polymers are the most widely used matrix materials and the two most common within the polymers are epoxy resin and polyester [2], being the specimen studied here composed by an epoxy resin.

### 2.1.3 Textile Composites

Over time, these type of composites have gain more and more importance in modern industry and are currently used in advanced structures in automobile, marine and aerospace industry, due to their mechanical properties, easy handle and low cost of the reinforced materials [8].

The mechanical properties of these materials are characterized by their anisotropy and inhomogeneous nature. As a consequence there are several parameters to take into account in order to control their mechanical properties such as fiber architecture, fiber properties, matrix properties, etc [8].

These composite are manufactured by impregnating matrix materials into their dry preforms in order to hold the multidirectional yarns together, using techniques such as: RTM (resin transfer molding), SRIM (structural reaction injection molding) and RFI (resin film infusion) [8].

Textiles composites can be distinctly separated in three structural levels: microscale, mesoscale and macroscale.

Textiles can also be classified in three different categories: woven fabrics, knitted fabrics and braided fabrics. Woven fabrics are the most widely and most commonly used in structural applications, and these are the materials that will be studied in the present dissertation.

#### 2.1.3.1 Woven fabrics

Woven fabrics are manufactured using the multiple warp weaving method, which consists of two sets of interlaced yarn components (one is called warp and the other weft, according to the yarn orientation). The mostly used woven fabrics in textile composites are the 2D fundamental weaves, for example plain, twill and satin weaves. Each one is identified by the repeating patterns of the interlaced regions in the warp and weft directions [8]. The three types of woven fabrics previously discussed are presented in Figure 2.2.

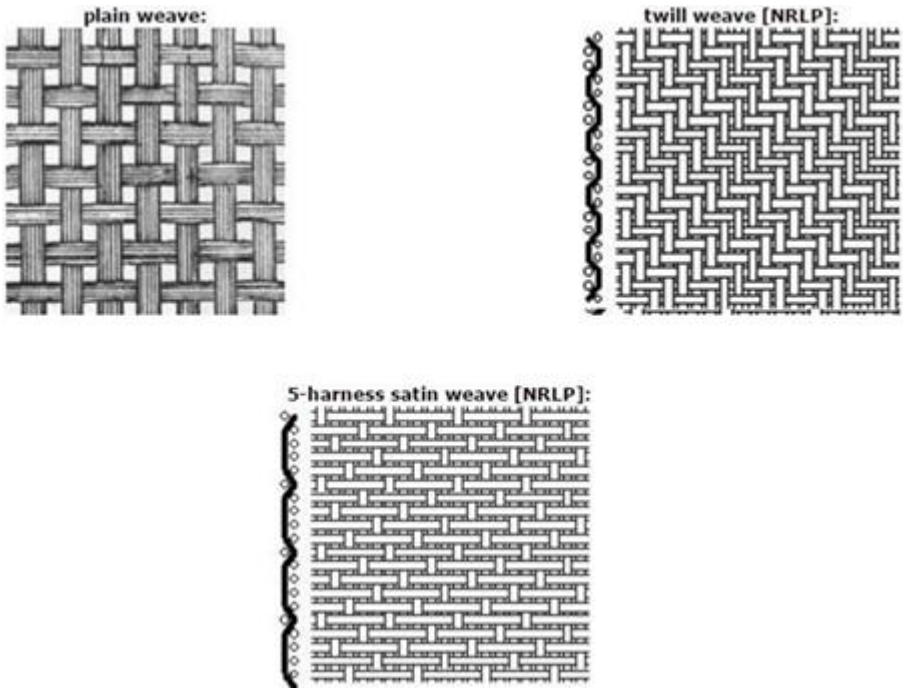


**Figure 2.2-**Representation of the different types of woven fabrics [9]

##### 2.1.3.1.1 Spread tow carbon fabric

CFRP composites presently evolving rapidly, as a result of the research and development being done nowadays. One of the main goals is to obtain lighter composites structures, as well as improving their performance/cost ratio, which may be interpreted as significant increase in properties with no additional cost. In order to make lighter structures, a recent method was developed called spread-tow technology. Figure 2.3 represents an example of this technology implemented in a carbon fabric. As recent studies show [10], the use of this technology allows us to get thinner plies, which is very important due to the key role of the thickness in controlling the mechanical properties of the composite material. In this study, the carbon fiber tow was thinned by increasing the tow width from 5 mm to 25 mm, which resulted in a reduced weight per unit area by approximately 500% [10], as well as an increase in the composite's mechanical properties.

**Figure 2.3 -** Sample of a spread-tow carbon fabric [11]

This tow-spreading technology consists of passing a tow through a spreading machine that is equipped with an air duct and a vacuum that sucks the air downward through the air duct. The use of this technology allows the production of unidirectional plies or woven fabric plies [1,8].

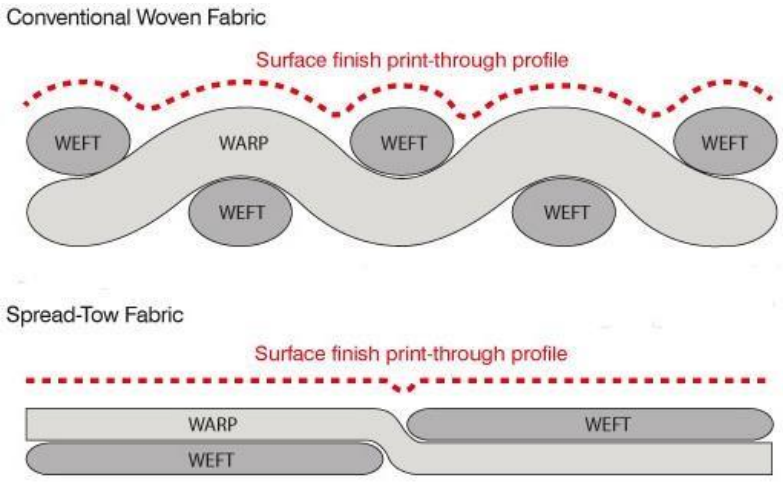


**Figure 2.4 -** Comparison between a conventional woven fabric and a spread-tow fabric [12]

#### 2.1.3.2 Pre-peg

Pre-peg is a term for pre-impregnated composite fibers where the matrix material, such as epoxy resin, is already present. The resin can be partially cured and in this form, is supplied to the manufacturer who can use it to lay-up a part. The reinforcement materials used in a pre-peg can either

be a fabric or unidirectional, and the two main methods of producing them are: hot melt and solvent dip.

The use of these materials can provide great advantages over conventional resin deposition during final production of the composite, due to the precise control of the ratio of fiber-resin, controlling the flow of resin during the curing process and in some processes, better control of the orientation and positioning of the fibers [1].

In this dissertation, the models consist of a spread tow carbon fabric pre-impregnated with an epoxy resin.

## 2.2 Constitutive Law's for Composite Materials

Composite are very complex materials and most of them either have an anisotropic or an orthotropic behavior.

In the case of an anisotropic material, its properties are different in all directions. These materials can, sometimes, result from the combination of two isotropic materials, which are a materials whose properties are assumed to be uniform in all directions. For example, when given two isotropic conducting materials, like a metal with high conductivity and a plastic that is electrically insulating, combining the two materials in alternating layers results in a highly anisotropic composite [13]. The anisotropic behavior of a material can vary in different ways and when subjected to applied loads, the actual deformation will depend on the material [6].

As stated by George H. Staab [6] for an orthotropic material, its properties are different in three mutually perpendicular planes. However, contrary to an anisotropic material, there is generally no shear-extension coupling. Because Poisson's ratio is different in the in-plane and out-of-plane directions, the respective transverse displacements are not typically the same. Figure 2.5 represents the response of an isotropic, anisotropic and orthotropic material when subjected to axial tensions. Although the response of the orthotropic materials appears similar to the isotropic material, the magnitudes of the in-plane and out-of-plane displacements are different [6].

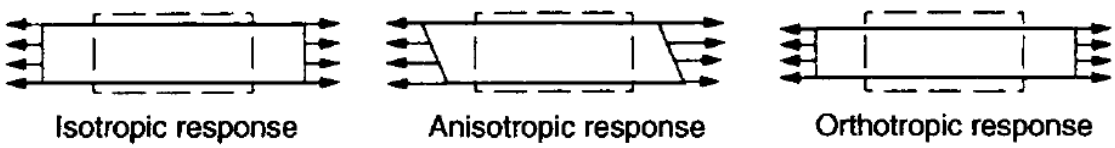


**Figure 2.5-** Typical behavior shown by isotropic, anisotropic and orthotropic material subjected to axial tension [6]

The fibers of the CFRP plate that are being studied in this dissertation are considered to have an anisotropic behavior, however they can also be considered to have a transverse isotropic behavior. For a transversely isotropic material, in addition to the three planes of symmetry, there is an axis of material symmetry. Thereby, any two material fibers having symmetrical positions with respect to the axis of symmetry have the same stiffness [6]. For example, a cell of a unidirectional composite material can be considered as being constituted by a fiber embedded in a cylinder of matrix, resulting in a material with an orthotropic behavior, having an axis of revolution in addition, which classifies this material as transversely isotropic, represented in Figure 2.6 [14].

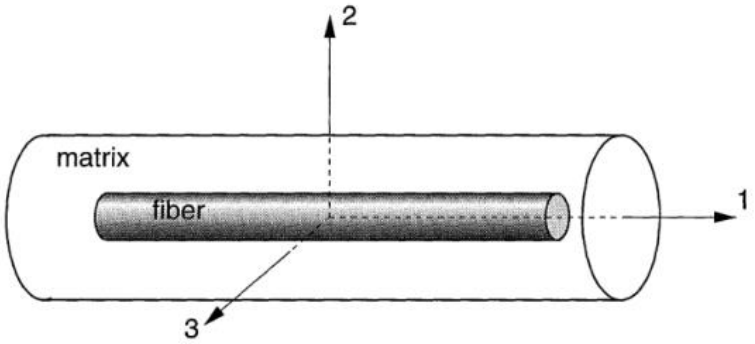


**Figure 2.6-** Unidirectional composite material constituted by the fiber and matrix [14]

### 2.2.1 Hooke's Law

In this area, it is very important to know the relation between stress and strain. However, this relation depends on the type of material under consideration. For specimens considered to have an elastic behavior, this relation is known as Hooke's law.

For orthotropic materials, the compliance matrix $[S]$ is expressed in the following form [15]:

$$[S] = \begin{bmatrix} \frac{1}{E_1} & -\frac{v_{21}}{E_2} & -\frac{v_{31}}{E_3} & 0 & 0 & 0 \\ -\frac{v_{12}}{E_1} & \frac{1}{E_2} & -\frac{v_{32}}{E_3} & 0 & 0 & 0 \\ -\frac{v_{13}}{E_1} & -\frac{v_{23}}{E_2} & \frac{1}{E_3} & 0 & 0 & 0 \\ 0 & 0 & 0 & \frac{1}{G_{23}} & 0 & 0 \\ 0 & 0 & 0 & 0 & \frac{1}{G_{31}} & 0 \\ 0 & 0 & 0 & 0 & 0 & \frac{1}{G_{12}} \end{bmatrix}, \quad (2.1)$$

where $E_1$, $E_2$ and $E_3$ are *Young's moduli* in directions 1, 2 and 3, respectively. $v_{ij}$ are Poisson's ratio and $G_{23}$, $G_{31}$ and $G_{12}$ are the *shear moduli* in the 2-3, 3-1 and 1-2 planes, respectively.

Given the symmetry of the compliance matrix, i.e. $S_{ij} = S_{ji}$ [15]:

$$\frac{v_{ij}}{E_i} = \frac{v_{ji}}{E_j}, i, j = 1,2,3. \tag{2.2}$$

Therefore, the stress-strain relation for orthotropic linear elastic materials can be expressed as,

$$[\varepsilon] = [S][\sigma]. \tag{2.3}$$

## 2.3 Multi-scale Models

The knowledge of fiber reinforced composite materials has increased over the last decades. Due to their microscopic heterogeneity, as well as the randomness of the fiber's positions, their bounding with the matrix and the presence of microdefects, the damage and non-uniform behavior of these composites, when subjected to external loads, becomes very complex and hard to predict [16]. In the field of composite materials, the study of these physical phenomenons takes a huge role. Physical phenomena can be characterized by a hierarchy of different complex models which are better suited at the appropriate scales, represented in Figure 2.7. As stated by Wan, Sun and Gu [17], *"The multi-scale models can be defined as constitutive models in which the global constitutive behavior of composite material is determined simultaneously throughout the analysis based on the behavior of the constituents and their interactions"*. These models provide a solid structure, based on fundamental principles, in order to develop mathematical and computational models of such phenomena [18].

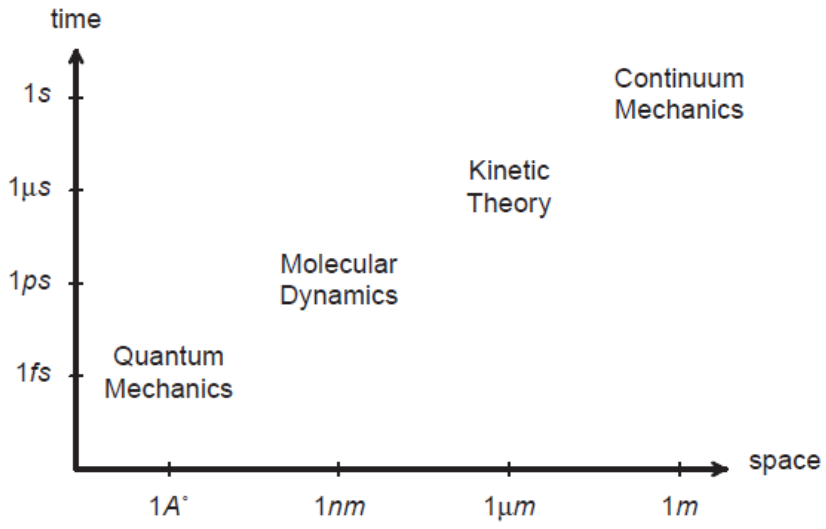


**Figure 2.7**-The different models at different scales [18]

Nowadays, when using finite element method (FEM) models to study these composites, different scales can be considered. These models can reach from micro unit cell models for crack propagation analysis to models with complete structural part made of composite material [19]. The most common levels are: microscale, mesoscale and macroscale. The first one defines the arrangement of the fiber, the mesoscale presents the fabric structure and fiber bundle and the macroscale works as a bounding mechanism between the unit cell and the engineering structure. Figure 2.8 represents the different scale levels as well as their respective features [20].

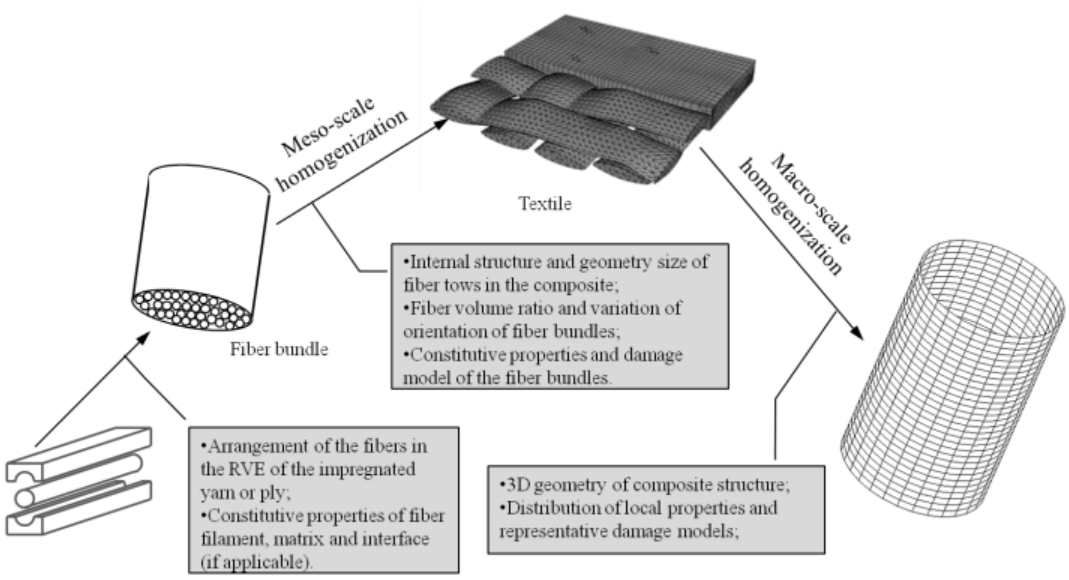


**Figure 2.8-** Representation of the three different scales and their respective features [20]

### 2.3.1 Microscale Models

As stated by Zhang [20], microscale models allow the forecast of the properties of the transversely isotropic unidirectional laminate. These models are always based on a representative volume element (RVE). As previously presented in Figure 2.8, at a microscale level, the fibers are embedded in matrix materials in order to form a yarn and a tow. The main objective of this scale is to compute the stress redistribution surrounding the broken fibers with different interfacial deformation models and, from these tests, obtain the average stress concentrations induced around the unbroken fibers and the stress recovery throughout the broken fiber [16].

Although this approach presents a good solution in order to approximately predict the properties of the unidirectional lamina, when modelling textiles and more complex composites the resort to this scale becomes uncommon due to the higher numerical cost when compared with the two approaches that will be described next, the macroscale and mesoscale models [19].

### 2.3.2 Mesoscale Models

At the meso level, the fiber bundles are composed by micro level composites. The laminate is considered homogeneous and the material orthotropic or transversely isotropic [2].

The main feature of these models is the realistic mesh, homogenized properties of the impregnated tows and the accurate definition of boundary conditions. At this level the analysis leads to non-uniform stress distributions over the unit cell, different from the ones obtained by most of microscale approaches [20].

This approach is used in order to predict the damage and failure of each constituent and their respective contribution to the global behavior. For this reason Inês Crespo implemented these mesoscale models in her dissertation, [2], and will also be implemented in the numerical simulations which will be presented throughout this dissertation.

### 2.3.3 Macroscale Models

The main objective of macroscale modeling approach is to extract and analyze the response of large structures using the results obtained from the mesoscale homogenization. This approach becomes a resourceful tool when using finite element tools and rely on Classical Laminate Plate Theory [20]. At this level the structural composition of the composite material is simplified. The material is considered homogeneous with properties equivalent to the composite in question [21].

The computational cost inherent to modeling at a macro level is significantly lower when compared with microscale and mesoscale, which allows the study of complex structures with larger dimensions.

The main drawback of this approach is the lack of micromechanical information about the interaction between the constituents and their individual failure contribution to the failure of the ply and the laminate [21].

## 2.4 Damage in Composite Materials

As previously mentioned, the role of composites in large and complex structures has been increasing over the last decades due to their properties, for example their relation between resistance/weight and the ability to manufacture components of complex geometries. As a consequence, these structures must be analyzed and tested periodically in order to guarantee its integrity and those of the composite elements [22].

Studies show that polymeric composites, which are mostly used in the aerospace industry, have the tendency to present different types of damage during their operational life time, as a consequence of their complex internal structure. Damage like delamination, inclusions, voids, resin-rich and resin starvation can occur during the process of manufacturing composite materials, whereas during their operational life, damage can occur due to service loads or impacts. As a consequence of these different types of damage the structures' operational life decreases significantly as well as their residual strength [22].

However, this does not mean the material failed. As stated by Crespo [2], damage is a physical discontinuity in the material, but it does not, necessarily, mean that the material can no longer be used. Only when the external loads are too high, the composite will fail leading to the laminate's fracture, i.e. rupture of the plies [21].

### 2.4.1 Failure Modes

Different types of failure modes related to the plies will be described here and are based on Maimí's PhD thesis [23] and Crespo's dissertation [2].

When testing a ply composed by unidirectional fibers impregnated with a polymeric matrix without notches, by applying various loads in the plane ($\sigma_{11}$, $\sigma_{22}$ and $\sigma_{12}$), the material will fail in a manner and under certain stresses. The bounding of all these points where the material fails under different stress states generate a failure surface, known as failure criteria. All the stress states present within this surface do not compromise the material's structural integrity, while the ones present outside the surface do [1,21]. It should be noted that within the composite materials there are many different failure modes, and these modes come from a different number of mechanical defects that cause failure of the material.

As presented in Figure 2.9, consider the fibers of the ply oriented in the direction 1. In the same figure, to the right, is represented the different fracture surfaces subjected to certain stress states.

Due to the material's geometry, five uniaxial test can be performed: traction and compression in the fiber direction ($\sigma_{11}$) and in the fiber's perpendicular direction ($\sigma_{22}$) and pure shear test ($\sigma_{12}$). For each of the tests, the failure stresses are, respectively, represented by $X_T$, $X_C$, $Y_T$, $Y_C$ and $S_L$, and the deformations are obtained by constitutive laws. Until failure occurs for the applied loads in the fiber direction and for the transverse traction loads, the behavior of the material is considered linear elastic, while for transverse compressive loads and pure shear the material is considered to have a nonlinear behavior before fracture occurs[23].

Experimental studies have led to the conclusion that, for unidirectional plies under plane stress conditions, four failure modes can be observed: longitudinal tensile fracture, longitudinal compressive fracture, transverse fracture with $\alpha = 0$ and transverse facture with $\alpha \neq 0$, respectively represented to the right of Figure 2.9 from top to bottom. The variable $\alpha$ represents the fracture angle, which is the measure between the plane of the fracture and the thickness direction of the laminate [2].

The stress states that generate each of the damage modes previously mentioned are also represented, $F_{\alpha=0}$, $F_{\alpha\neq0}$, $F_{FT}$ and $F_{KB}$, in the planes $\sigma_{11} - \sigma_{22}$, $\sigma_{11} - \sigma_{12}$ and $\sigma_{22} - \sigma_{12}$. $F_{\alpha=0}$ and $F_{\alpha\neq0}$ correspond to the transverse failure modes, while $F_{FT}$ and $F_{KB}$ correspond to the longitudinal failure modes [23].

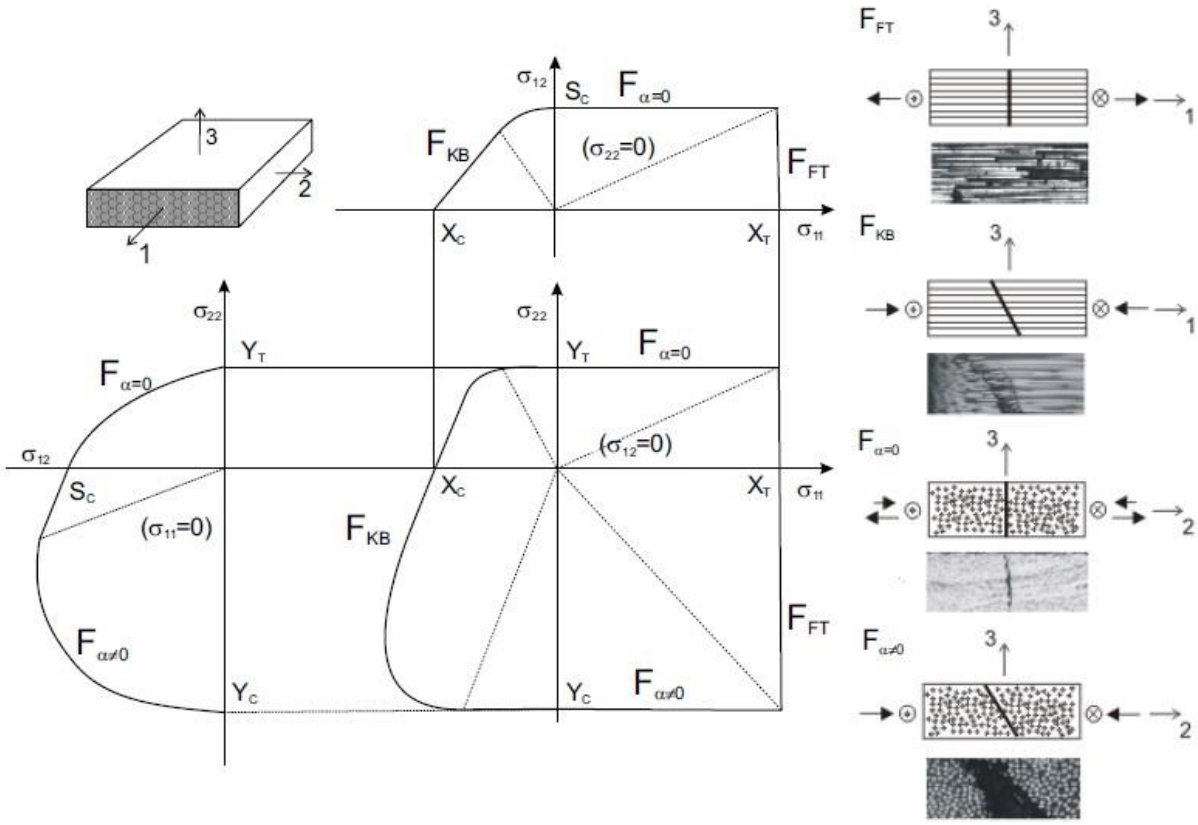


**Figure 2.9-** Fracture surfaces for each state of stress and the four main failure modes [23]

#### 2.4.1.1 Longitudinal tensile fracture

Most of the applied loads are transferred to the fibers, for these act as the reinforcement of the composite material. When these fibers fail, the loads are then redistributed to other areas of the structure, i.e. to the adjacent fibers and matrix. The transfer between the interface and the matrix will lead to a significantly increase of loads in the neighboring, which might compromise the composite's structural integrity, causing cracks in the material and debonding of the plies. In this failure mode, failure can occur in both fibers and matrix [2].

In Figure 2.9 it can be observed that when applying these types of tensions, the failure occurs transversally to the fibers of the laminate.

#### 2.4.1.2 Longitudinal compressive fracture

Longitudinal compressive fracture is the most complex failure mode between the four presented here. When a laminate is significantly subjected to compressive loads in the fiber direction, the failure of the respective laminate commonly occurs due to the generation of kink bands. Although this is the most common failure mode, the same can occur due to micromechanical phenomenons like microbuckling or fiber crushing and the distinction between this modes is important.

Microbuckling is a micromechanical fiber failure that consists in geometric instabilities localized in the fibers that cause transverse displacements when the laminate is subjected to compressive loads. The first theoretical analysis of this type of failure as a phenomenon of elastic instability was developed by Rosen [24]. However the results showed failure stresses higher than the ones usually observed experimentally. Since then, most researchers have been using Rosen's models in order to study this phenomenon.

According to Maimí [23], kink bands relate to the last stage of longitudinal compressive failure. However the formation of kink bands is very complex and there's yet a lot of discussion on this matter. Pinho [25] considers that kink bands usually initiate in regions of large fiber misalignment, as represented in Figure 2.10. This misalignment in the fibers, when subjected to compressive loads, will result in their rotation which leads to shear stresses in the matrix. As a consequence the matrix fails which leads to a further rotation of the fibers. This excessive rotation then causes the formation of kink bands.

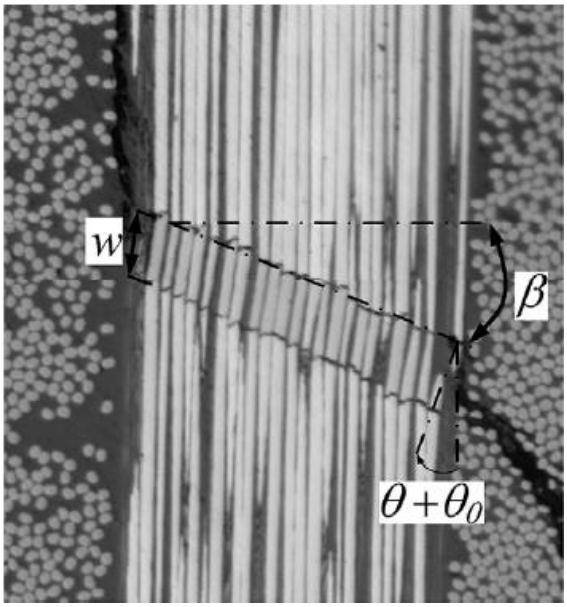


**Figure 2.10-** Usual kink band geometry [25]

#### 2.4.1.3 Transverse fracture ($\alpha = 0$)

This type of failure mode occurs under transverse tension and in plane shear loads, as well as under high shear stresses and moderate values of transverse compression. When under transverse tensions or in-plane shear loads, the fracture occurs transversely to the laminate [23].

#### 2.4.1.4 Transverse fracture ($\alpha \neq 0$)

This failure mode is very similar to the previous one, being the difference the fracture angle no longer being zero. This occurs when the transverse compressive loads applied to the laminate are significantly increased. According to Puck [23,24], when under pure transverse compressive stressing the fracture angle $\alpha$ is proximally $53° \pm 3°$. However, if the test is under pure transverse compressive loads and at the same time in-plane shear loads, the fracture angle decreases to $40°$.

In fact, under transverse compressive loads, the fracture angle varies with the compression's strength intensity and shear, increasing when the applied loads are higher, while the intensity of the in-plane shear stress causes a decrease in the fracture angle.

### 2.4.2 Failure Criteria

Failure criteria are analytical functions that are used in order to predict failure of the laminate and thus the respective stress values that caused it to fail. As previously mentioned, these criteria determine the failure of the composite material by using the failure stresses obtained from the five uniaxial tests.

In the next sub chapters some of the most common and used failure criteria will be presented and explained, as well as some failure criteria implemented in LS-DYNA.

#### 2.4.2.1 Maximum strain

This is one of the most simple and direct criteria used to predict failure [28]. This criterion contemplates that the laminate will fail when the strain exceeds a certain, allowable value.

Failure can occur in three different conditions, consisting in the maximum strain in fiber direction, matrix direction and shear strains:

$$\begin{aligned} \varepsilon_1 \geq \varepsilon_{1T}^u \quad &\text{or} \quad |\varepsilon_1| \geq \varepsilon_{1C}^u \\ \varepsilon_2 \geq \varepsilon_{2T}^u \quad &\text{or} \quad |\varepsilon_2| \geq \varepsilon_{2C}^u \\ \varepsilon_{12} \geq \varepsilon_{12T}^u \, , & \end{aligned} \tag{2.4}$$

$\varepsilon_{1T}^u$ and $\varepsilon_{2T}^u$ are the tensile normal failure strain in the 1 (fiber direction) and 2 (matrix direction) direction, respectively, $\varepsilon_{1C}^u$ and $\varepsilon_{2C}^u$ are the compressive normal failure strains as well in the 1 and 2 direction and the last, $\varepsilon_{12T}^u$, is the laminate shear strain failure in the 12 plane.

#### 2.4.2.2 Maximum stress

This criteria is, in some way, very similar to the maximum strain failure criterion with the exception of using stresses instead of strains in order to predict laminate failure. This way, the laminate fails when the stress exceeds a certain allowable value. Failure can occur by either of the following conditions:

$$\begin{aligned} \sigma_1 \geq X_T \quad &\text{or} \quad |\sigma_1| \geq X_C \\ \sigma_2 \geq Y_T \quad &\text{or} \quad |\sigma_2| \geq Y_C \\ |\sigma_{12}| \geq S_{12} & \end{aligned} \tag{2.5}$$

where $\sigma_1$ represents the stress of the lamina in the fibers direction, $\sigma_2$ represents the stress in the transversal direction of the fibers and $\sigma_{12}$ represent the in-plane shear stress.

$X_T$ and $Y_T$ are the tensile normal strength in the 1 (fiber direction) and 2 (matrix direction) direction, respectively, $X_C$ and $Y_C$ are the compressive normal strength as well in the 1 and 2 direction and the last, $S_{12}$, is the laminate shear strength in the 12 plane.

#### 2.4.2.3 Hashin

This criterion considers four conditions in order to distinguish failure of the fibers and the matrix under a three-dimensional state of stress. In the fiber failure mode under tensile loads, the effect of the shear stresses are taken into account and for the matrix failure mode a quadratic approach is considered [28]. Failure occurs upon the following conditions:

Tensile fiber mode ($\sigma_1 > 0$):

$$\left(\frac{\sigma_1}{X_T}\right)^2 + \frac{\sigma_{12}^2 + \sigma_{13}^2}{S_{12}^2} \geq 1 \tag{2.6}$$

Compressive fiber mode ($\sigma_1 < 0$):

$$|\sigma_1| \geq X_C \tag{2.7}$$

Tensile matrix mode ($(\sigma_2 + \sigma_3) > 0$):

$$\left(\frac{\sigma_2 + \sigma_3}{Y_T}\right)^2 + \frac{\sigma_{23}^2 + \sigma_2\sigma_3}{S_{23}^2} + \frac{\sigma_{12}^2 + \sigma_{13}^2}{S_{12}^2} \geq 1 \tag{2.8}$$

Compressive matrix mode ($(\sigma_2 + \sigma_3) < 0$):

$$\left[\left(\frac{Y_C}{2S_{23}}\right)^2 - 1\right]\frac{\sigma_2 + \sigma_3}{Y_C} + \left(\frac{\sigma_2 + \sigma_3}{2S_{23}}\right)^2 + \frac{\sigma_{23}^2 + \sigma_2\sigma_3}{S_{23}^2} + \frac{\sigma_{12}^2 + \sigma_{13}^2}{S_{12}^2} \geq 1 \tag{2.9}$$

$S_{23}$ represents the shear strength in the 23 plane. All the other variables are the same and already described in the previous failure criteria.

This criterion was proposed posteriorly to the Hashin-Rotem failure criterion, however, unlike the latter, Hashin's criterion is not able to formulate kink bands [28].

#### 2.4.2.4 Tsai-Wu

This is a type of failure criterion that is not associated with failure modes, which means that this criterion does not allow to identify in which mode failure occurred. Also, directions 1, 2 and 3 are not considered aligned with the principal directions.

This criterion is presented as a further development of the Tsai-Hill failure criterion, in which tensile and compressive strength are distinguishable [21] and it is also one of the most direct criteria, for only consider one polynomial equation, expressed as [28]:

$$F_i\sigma_i + F_{ij}\sigma_i\,\sigma_j + F_{ijk}\sigma_i\sigma_j\sigma_k \geq 1$$

As stated by Kozub [21] for a transversely isotropic material under biaxial stress state, failure occurs by the following condition:

$$\left(\frac{1}{X_T}-\frac{1}{X_C}\right)\sigma_1 + \left(\frac{1}{Y_T}-\frac{1}{Y_C}\right)\sigma_2 + \frac{\sigma_1^2}{X_T X_C} + \frac{\sigma_2^2}{Y_T Y_C} + \frac{\sigma_{12}^2}{S^2} - \sqrt{\frac{1}{X_T X_C Y_T Y_C}}\,\sigma_1\sigma_2 \geq 1 \qquad (2.10)$$

#### 2.4.2.5 Chang-Chang

As Zarei [29] stated *"Chang-Chang failure criterion is a modified version of the Hashin failure criterion in which the tensile fiber failure, compressive fiber failure, tensile matrix failure and compressive matrix failure are separately considered."*. This modification was made in order to include the non-linear shear stress-strain behavior of a composite lamina.

Chang and Chang [30] developed a two dimensional failure criterion for unidirectional laminas with the following conditions:

Tensile fiber mode:

$$\text{If } \sigma_1 > 0 \quad \text{then} \quad \left(\frac{\sigma_1}{X_T}\right)^2 + \frac{\sigma_{12}}{S_C} = 1 \qquad (2.11)$$

Compressive fiber mode ($\sigma_1 < 0$)

$$\text{If } \sigma_1 < 0 \quad \text{then} \quad \left(\frac{\sigma_1}{X_C}\right)^2 = 1 \qquad (2.12)$$

Tensile matrix mode ($\sigma_2 > 0$)

$$\text{If } \sigma_2 > 0 \quad \text{then} \quad \left(\frac{\sigma_2}{Y_T}\right)^2 + \left(\frac{\sigma_{12}}{S_c}\right)^2 = 1 \qquad (2.13)$$

Compressive matrix mode ($\sigma_2 < 0$)

$$\text{If } \sigma_2 < 0 \quad \text{then} \quad \left(\frac{\sigma_2}{2S_C}\right)^2 + \left[\left(\frac{Y_C}{2S_C}\right)^2 - 1\right]\frac{\sigma_2}{Y_C} + \left(\frac{\sigma_{12}}{S_c}\right)^2 = 1 \tag{2.14}$$

$S_C$ represents the in-plane shear strength. All the other variables are the same and already described in the previous failure criteria.

Summarizing the failure criteria previously described, two main categories can be identified: failure criteria not associated with failure modes and failure criteria associated with failure mode.

The first one takes into account all polynomial and tensorial criteria by using mathematical expressions in order to describe the failure surface as a function of the material strengths. This category as some advantages, such as the invariance under rotation of coordinates. However, there are some drawbacks as well as the inability to identify the different damage mechanisms that lead to failure of the laminate and the inability to deal with the non-homogeneity character of composites. As previously stated, the Tsai-Wu criterion is included in this category, such as Tsai-Hill and other failure criteria that won't be described in this dissertation.

The second category refers to criteria such as, maximum strain, maximum stress, Hashin and Chang-Chang. Contrary to the former, these criteria take into account the non-homogeneity character of composites and can predict the different failure modes.

## 2.5 Testing and Certification

Materials are in constant development, which, as a consequence, lead to the desire of an engineer to predict the behavior and performance of a certain future material. The resource that is used in order to test and certify advanced composite materials is the multivolume U.S. Department of Defense (DoD) *Composite Materials Handbook*, Military Handbook 17 (MIL-HDBK-17) [1].

As stated, composites are very complex materials whose behavior differs from the ones observed in some isotropic materials. Before testing a certain material, the one responsible for that material must take into account the following considerations [1]:

- *"The difference between testing composite and isotropic materials;*
- *The key role of certification agencies ;*
- *The building-block approach;*
- *Determine the whole purpose of testing;*

- *Need to normalize results;*
- *Application of basics statistics;*
- *Other factor that will influence the design allowable".*

The building-block approach becomes a key tool with great importance, due to the combination between the difficulty of testing a composite material and its lack of validation and widely applicable methods of pattern analysis.

In Figure 2.11 the concept of the building-block approach is illustrated. In the first level (the lowest level) the properties of the basic composites are determined through a large number of test specimens. At each level, more complex structures are developed and tested in a progressive way, recurring to the test data obtained by the lower levels in order to predict the failure mode. As the structures progressively become more complex, the number of test specimens and the number of environment decreases [1].

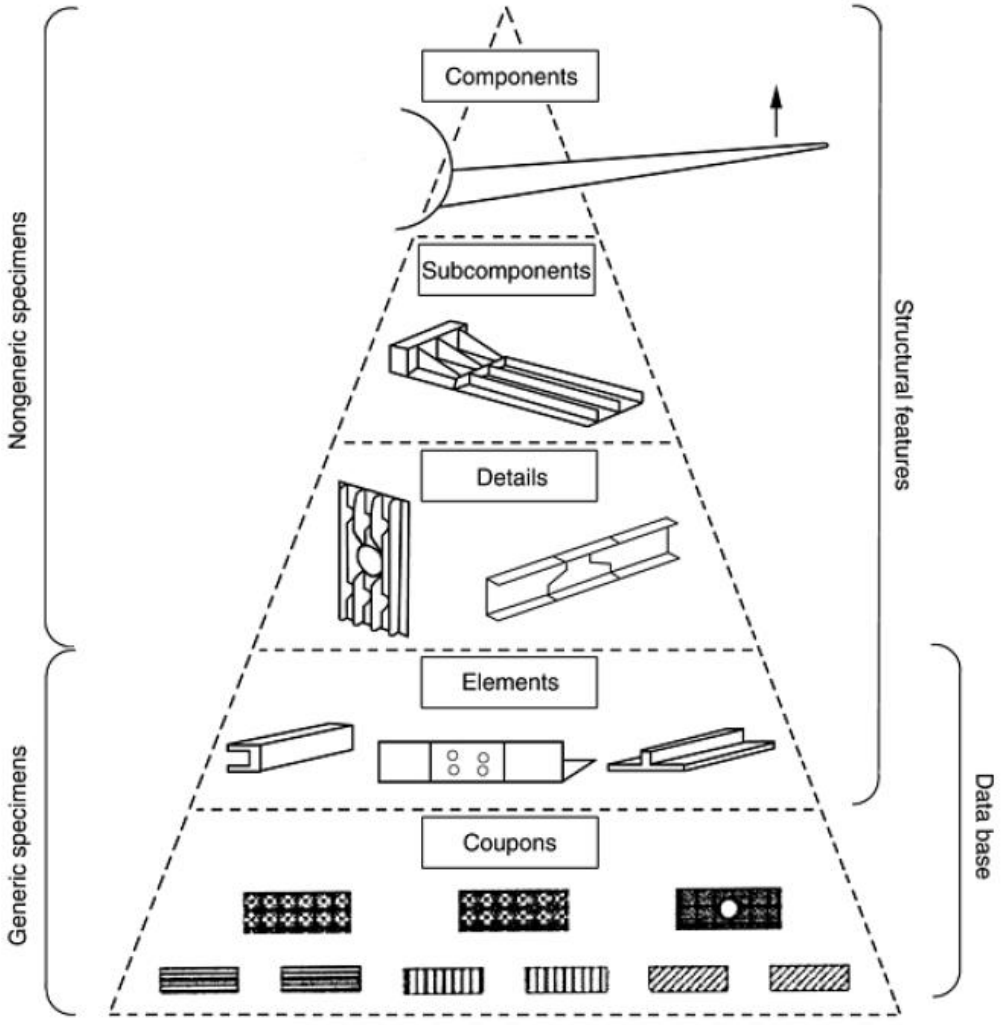


**Figure 2.11-** The building-block approach represented in a pyramid [1]

## 2.6 Dynamic Analysis – General Considerations

Hamilton's principle is a generalization of the principle of virtual work to the dynamic of solid bodies [31]. According to this principle any system is considered to have two types of energy, total potential and kinetic energy. In order to achieve balance, the principle states that the system must be stationary and must satisfy the following condition:

$$\int_{t_1}^{t_2} (T - \pi) dt \tag{2.15}$$

where $T$ represents the kinetic energy and $\pi$ represents the total potential energy. From this principle we obtain the following equations of dynamic balance [31]:

$$\frac{\partial}{\partial t}\frac{\partial T}{\partial \dot{u}} + \frac{\partial \pi}{\partial u} = 0 \tag{2.16}$$

where,

$$\dot{u} = \frac{\partial u}{\partial t} \tag{2.17}$$

Substituting the discretized equations of kinetic, deformation and potential energy in the equation of dynamic balance, we obtain the following expression:

$$M_{JK}\ddot{u}_k + K_{JK}u_k = F_J \tag{2.18}$$

It should be noted that the general equation of dynamic balance takes into account the dissipated energy caused by the damping, i.e.:

$$M_{JK}\ddot{u}_k + C_{JK}\dot{u}_k + K_{JK}u_k = F_J \tag{2.19}$$

where $\ddot{u}_K$, $\dot{u}_K$ and $u_K$ represent the acceleration, velocity and displacement vectors of each node of the structure, respectively. $M_{JK}$, $C_{JK}$ and $K_{JK}$ represent the mass, damping and stiffness matrix, respectively. In the present dissertation, the case study belongs to a non-damped system, i.e., $C_{JK} = 0$. If harmonic motion is considered:

$$\begin{aligned} u_k &= \bar{u}_k sin(wt) \\ \dot{u}_k &= \bar{u}_k w cos(wt) \\ \ddot{u}_k &= -\bar{u}_k w^2 sin(wt) \end{aligned} \tag{2.20}$$

where $\bar{u}_k$ represents the amplitude of the sinusoidal vibration in the respective degree of freedom, $u_k$, it is possible to study harmonic vibrations. When the absence of external forces ($F_J = 0$) and damping is considered, substituting the previous expressions [31], the following expression is obtained:

$$\left(-w^2 M_{JK}\bar{u}_k + K_{JK}\bar{u}_k\right)\sin(wt) = 0 \tag{2.21}$$

Simplifying, we get:

$$\left(K_{JK} - w^2 M_{JK}\right)\bar{u}_k = 0 \tag{2.22}$$

This last equation represents a system of eigenvalues and eigenvectors. This system can be solved in order to determine the natural frequencies (eigenvalues) and the vibration modes (eigenvectors). When external forces applied to the system vary with time ($F_J \neq 0$) and the dissipated energy caused by damping is considered ($C_{JK} \neq 0$), by recurring to the explicit or implicit analysis, equation 2.19, it is possible to solve transient phenomenons, by integration over time [31]. Knowing the solutions of the acceleration, velocity and displacement vector from equation 2.19 for the instance $t$ and the acceleration vector for the instance $t + \Delta t$, using Taylor series, it becomes possible to estimate the velocity and displacement for the instance $t + \Delta t$ [32]:

$$u_{t+\Delta t} = u_t + \dot{u}_t \Delta t + \left[\left(\frac{1}{2} - \beta_2\right)\ddot{u}_t + \beta_2 \ddot{u}_{t+\Delta t}\right]\Delta t^2 \tag{2.23}$$

$$\dot{u}_{t+\Delta t} = \dot{u}_t + [(1-\beta_1)\ddot{u}_t + \beta_1 \ddot{u}_{t+\Delta t}]\Delta t^2 \tag{2.24}$$

The type of integration, whether is explicit or implicit, is determined by the parameters $\beta_1$ and $\beta_2$. If $\beta_1 = \beta_2 = 0$, integration will be purely explicit. If $\beta_2 = 0$, integration is explicit, however if $\beta_2 \neq 0$, integration is implicit [32]. Substituting the last two equations in the second one the accelerations for the instance $t + \Delta t$ can be calculated by using direct integration:

$$\begin{aligned}(M + \beta_1 C\Delta t + \beta_2 K\Delta t^2)\ddot{u}_{t+\Delta t} \\ = F_{t+\Delta t} - C[\dot{u} + (1-\beta_1)\ddot{u}_t\Delta t] - K\left[u_t + \dot{u}_t\Delta t + \left(\frac{1}{2} - \beta_2\right)\ddot{u}_t\Delta t^2\right]\end{aligned} \tag{2.25}$$

When comparing explicit with implicit analysis it is important to know the characteristics of each of these two types of integration. Resolution of equation 2.25 for the explicit integration scheme is very

simple and fast, due to the fact that a diagonal mass matrix can be used, which transforms equation 2.25 into a set of independent equations. This type of integration is conditionally stable and requires lower time intervals, $\Delta t$, than implicit integration. Implicit integration takes more time to solve as the combination of mass and stiffness matrixes can no longer be diagonalized. In this scheme it is necessary to solve a system of equations, for each of the time steps, in order to obtain $\ddot{u}_{t+\Delta t}$ [32].

When working with dynamic analysis using FEM's, the time step becomes an important parameter to take into account. In order to get a good numerical accuracy the time step should be as small as possible [33]. However, when using an explicit integration method, the critical time step must be taken into account and a time step close to the critical one usually results in the best numerical accuracy [33]. In LS-DYNA, the critical time step is computed from [3]:

$$\Delta t_c = \frac{L_c}{\left\{\left[Q + (Q^2 + c^2)^{\frac{1}{2}}\right]\right\}} \tag{2.26}$$

where $c$ is the adiabatic sound of speed and $Q$ represents a function of the bulk coefficients $C_0$ and $C_1$:

$$Q = \begin{cases} C_1 c + C_0 L_c |\dot{\varepsilon}_{kk}| & for\ \dot{\varepsilon}_{kk} < 0 \\ 0 & for\ \dot{\varepsilon}_{kk} < 0 \end{cases} \tag{2.27}$$

$L_c$ represents the characteristic length of an element, which for 8 node solids is obtained from:

$$L_c = \frac{v_c}{A_{c_{max}}} \tag{2.27}$$

where $v_c$ and $A_{c_{max}}$ represent the volume and the area of the largest side of the element, respectively [3].

## 2.7 Hourglass Control

As previously mentioned this dissertation involves dynamic analysis with explicit integration, which, when working with finite element methods (FEM), and in this case with element formulations with reduced integration, make the knowledge of what hourglass means, and how to inhibit or eliminate this phenomenon very important. Hourglass (HG) is mostly a nonphysical mode of deformation that results from the excitation of zero energy degrees of freedom that, as a consequence, produce zero strain and no stress [34].

This phenomenon occurs on reduced-integrated, i.e., single integration point or single in-plane integration point in the case of shell elements, two dimensional and three dimensional shell, thick shell and solid elements. In order to fully understand hourglass, in Figure 2.12 a deformation of an element with reduced integration subjected to pure bending is presented.

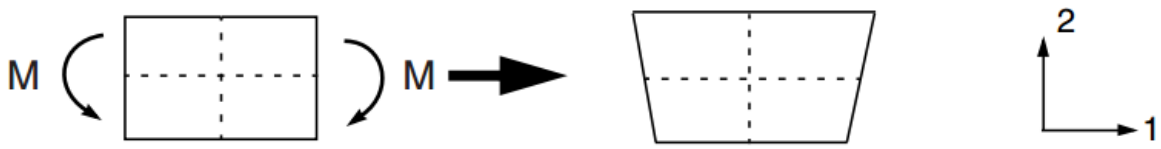


**Figure 2.12-** Demonstration of the deformation of an element with reduced integration when subjected to a bending load [35]

By observing the figure it can be concluded that the length and the angle between each of the dotted lines of the element, after being subjected to pure bending, has not changed, which means that the stresses at the single point of integration of the elements are zero [35]. As such, this nonphysical mode of deformation is a consequence of the bending mode which is a zero energy mode, since no strain energy is generated by this element's distortion [35].

When using LS-DYNA[2], a solution, in order to eliminate hourglass problems, is to use element formulations with full-integration or selectively reduced (S/R) integration. However, these formulations have some drawbacks such as high computational cost, instability in large deformation applications and the tendency to 'shear-lock', which is common in type 2 solid elements. Other solutions, in order to inhibit hourglass are mesh refinement, and the application of internal hourglass forces in order to resist the hourglass mode deformation. The last one is done by hourglass formulations available in LS-DYNA. The software used in this dissertation has two main features in order to control hourglass: *CONTROL_HOURGLASS and *HOURGLASS. When using the second feature, the global settings of the first one are overridden. Both features have two forms of control such as viscous forms, which generate forces proportional to components of nodal velocity and stiffness forms, which generate forces proportional to components of nodal displacement. However stiffness form control is usually more effective than viscous form control for structural parts [34].

[2] The definition of the element formulations are shown in the Appendix

For solid elements, three forms of viscous and two forms of stiffness hourglass control can be selected. For viscous control, there are type 1, which is the standard type and the one that takes the lowest computational cost, type 2, which is the Flanagan-Belytschko viscous form and type 3, which is the same as type 2 with exact volume integration. For stiffness control there are type 4 and type 5, which have the same formulation as 2 and 3, respectively, but for stiffness form. However, there are also four more type that are not included in the two previous forms of hourglass control. These are type 6, which is an assumed strain, co-rotational stiffness formulation by Belytschko-Bindeman,, type 7, which is variation of type 6 with a comparison between the deformed geometry and the original geometry, type 9, that may be considered as an enhanced type 6 and type 10, with a formulation Cosserat Point Element (CPE).

For shell elements, only one viscous and stiffness control can be selected, i.e., for viscous control types 1, 2 and 3 are identical and for stiffness control types 4, 5 and 6 are also identical. However, when using shell element formulation 16, hourglass control type 8 can be selected, which activates the full projection warping stiffness for accurate solutions. In Table 2.1 is depicted all the HG control types and, for each element type, which HG control is available to select.

**Table 2.1-** Hourglass control for each element type

| HG control type | Solid Element | Shell element |
|---|---|---|
| 1 | X | X |
| 2 | X | X |
| 3 | X | X |
| 4 | X | X |
| 5 | X | X |
| 6 | X | X |
| 7 | X | |
| 8 | | X[3] |
| 9 | X | |
| 10 | X | |

[3] For shell element formulation 16

# 3
# Numerical Analysis – Model Testing

In this chapter a study of delamination of a unidirectional ply cantilever beam model is described, constituted by a spread tow carbon fabric ply oriented at $0^0/90^0$ under dynamic tensile loads. This study was done in order to validate the numerical model used in LS-DYNA [3] using cohesive elements, with the objective of implementing the delamination phenomena in the final model where failure criteria is taken into account.

For both models, a linear elastic orthotropic material behavior is considered.

## 3.1 Delamination

The initiation and propagation of delamination is often one of the main contributors to ultimate failure in laminated composite structures[36], such as the ones being studied in this dissertation. Three different modes of separation can be observed when delamination occurs, which are represented in Figure 3.1: Mode I (opening mode), Mode II (in-plane shearing mode) and Mode III (tearing or scissoring sharing mode).

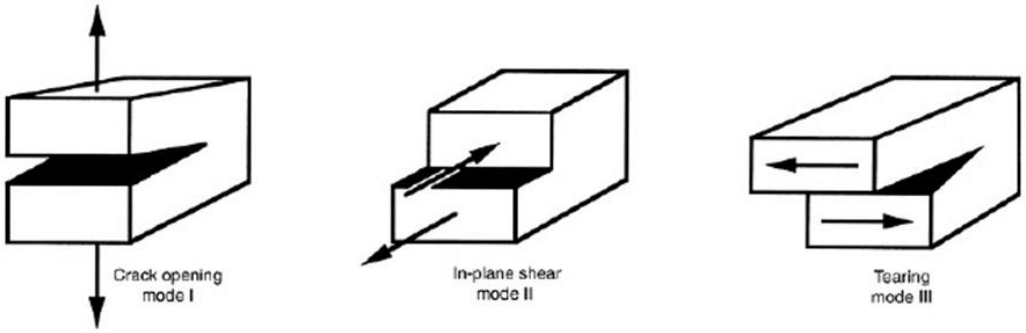


**Figure 3.1**-Three modes of delamination fracture [1]

The interlaminar fracture toughness (IFT) is a measure of the ability of a material to resist delamination. For each of the three different modes a critical strain energy release rate ($G_I, G_{II}, G_{III}$) is considered, and the combination of at least two modes is called mix mode [1].

Therefore, the knowledge of these particular failure modes and the ability to model them deserves particular attention and becomes very important in order to maintain structural integrity of composite structures.

Using LS-DYNA, delamination can be modeled by fracture mechanism based methods, stress based methods or by techniques such as Virtual Crack Closure Technique (VCCT), Tie-Break Interface (TBI) and Cohesive Zone Model (CZM).

In the present study, a CZM model is used in order to simulate delamination. LS-DYNA allows the user to access a large number of materials for the cohesive elements, such as *MAT_138, *MAT_184, *MAT_185 and *MAT_186 [37]. The model developed in this dissertation uses the *MAT_138, which is a bilinear traction-separation law for both Mode I (opening mode) and Mode II (in-plane shearing mode), as represented in Figure 3.2, with a quadratic mixed-mode delamination criterion and a damage formulation.

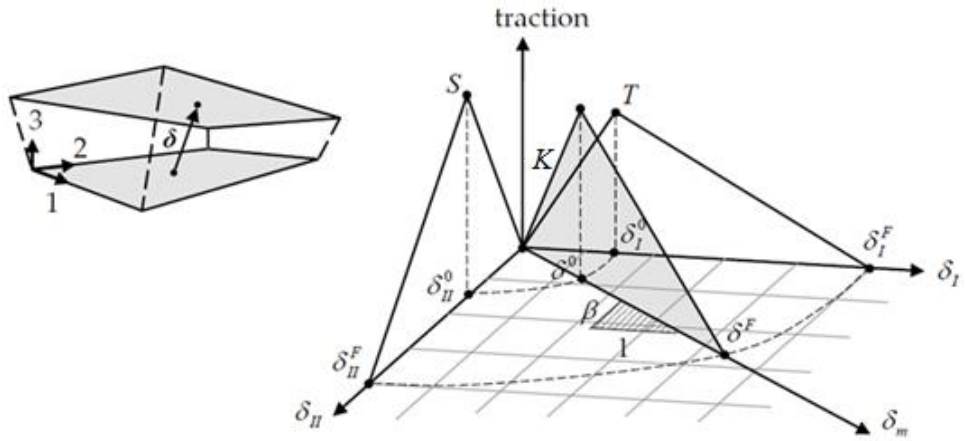


**Figure 3.2**-Mixed mode traction-separation law [37]

In bilinear models two stages are considered. The first and second stages refer to the loading and the unloading state, respectively. The slope of the stress-displacement curve corresponds to $K$ (represented in LS-DYNA's code as the variable $EN$ and $ET$, depending on whether it's the stiffness normal or in the plane of the cohesive element, respectively), which is the interfacial stiffness between plies and the area under the stress-displacement curve corresponds to the fracture toughness $G_c$.

Given that the test specimen will not be loaded under pure mode I or pure mode II, it is necessary to calculate a mixed-mode displacement from the single-mode displacements [38],

$$\delta_m = \sqrt{\delta_I^2 + \delta_{II}^2},$$

where

$$\delta_I = \delta_3$$

is the separation in the normal direction and

$$\delta_{II} = \sqrt{\delta_1^2 + \delta_2^2}$$

is the separation in the tangential direction.

The ultimate mixed-mode displacement $\delta_F$ (total failure) can be obtained by two different formulations:

- by the power law (XMU > 0)

$$\delta_F = \frac{2(1+\beta)^2}{\delta^0}\left[\left(\frac{EN}{GIC}\right)^{XMU} + \left(\frac{ET\times\beta^2}{GIIC}\right)^{XMU}\right]^{-\frac{1}{XMU}} \tag{3.1}$$

- by the Benzeggagh-Kenane law (XMU < 0)

$$\delta_F = \frac{2}{\delta^0\left(\frac{1}{1+\beta^2}EN + \frac{\beta^2}{1+\beta^2}ET\right)}\left[GIC + (GIIC - GIC)\left(\frac{\beta^2\times ET}{EN + \beta^2\times ET}\right)^{|XMU|}\right] \tag{3.2}$$

XMU and $\beta$ are two variables in LS-DYNA's code, the first being an exponent of the mixed mode criteria and the second is the "mode mixity" ($\beta = \delta_{II}/\delta_I$), which is represented in Figure 3.2.

Given that the delamination can occur for both Mode I (by normal stresses) or Mode II (by tangential stresses), and for Mode III (by normal and tangential stresses), it is possible to define bilinear relations between the normal stress, $\sigma_n$, and the displacement in the normal direction, $\delta_n$, and between the tangential stress, $\tau_t$, and the displacement in the tangential direction, $\delta_t$ as depicted in Figure 3.3. For both cases the stress-displacement relation is linear.

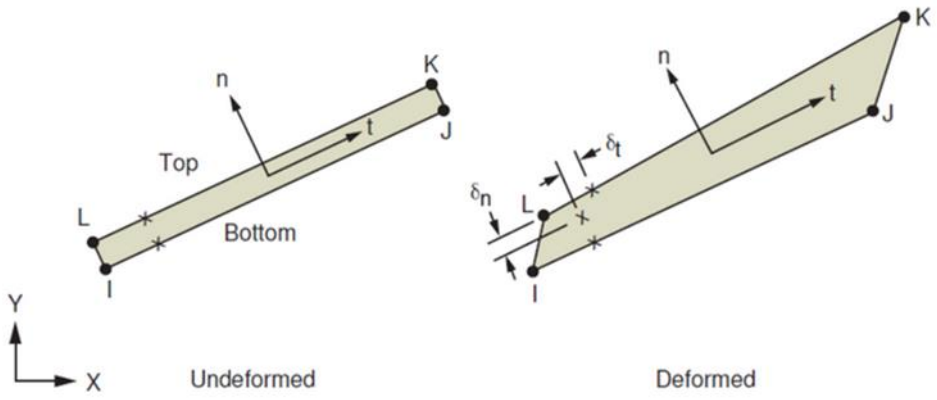


**Figure 3.3 -** Schematic of interface elements [39]

In order to validate the parameters of the chosen material model for the cohesive zone, a study of the delamination of an unidirectional ply model is carried out using a double cantilever beam (DCB) specimen, represented in Figure 3.4.The results of the numerical model are compared with the ones obtained by experimental testing reported by Turon et al [40].

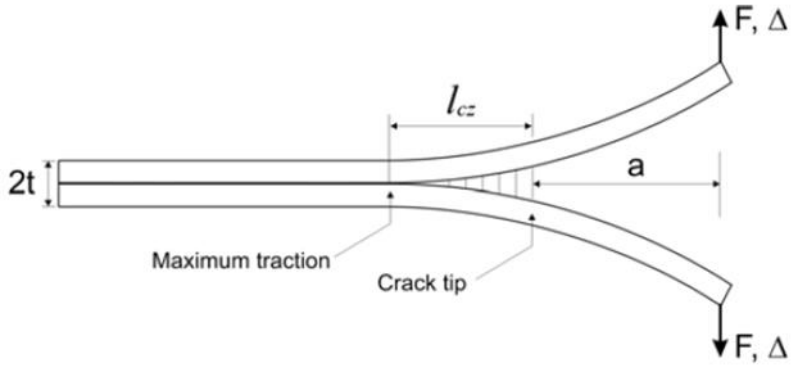


**Figure 3.4 -** DCB specimen [41]

### 3.1.1 Delamination Analysis and Results

In the present study, it is important to define the type of element that is used to model the test specimen. LS-DYNA has available a large number of elements types, but for this model only two are of interest: thick-shells and solids. Preliminary studies conducted by Muflahi, Mohamed and Hallett [42] demonstrate that between element formulation 1, 2 and 5 for thick-shell elements and element formulation 1 and 2 for solid elements, the last ones lead to results with better balance in

stiffness, initiation of delamination and running times. The definition of these element formulations and the ones that will be described next are shown in the Appendix. In this study both elements (8-node hexahedron solid and thick-shell elements) are implemented in the model and compared with the results presented in [40] and the ones obtained in Mangualde's work. Figure 3.5 represents the test specimen, with the implementation of solid elements (two unidirectional plies) and an initial crack length of 55 mm that is modeled in LS-DYNA, taken from [40]. The boundary conditions are also represented, with one end fixed and the other with a displacement, $\delta_z$, of 5 mm imposed in the *z*-direction. The boundary conditions for the model with thick-shell elements are the same, except for the addition of a constrain in the y-direction in the two faces transverse to the width of the test specimen in order to avoid element distortion. The model has 1500 elements long, 1 wide and 2 thick, instead of the 1 element thick that Crespo implemented in her model [2].

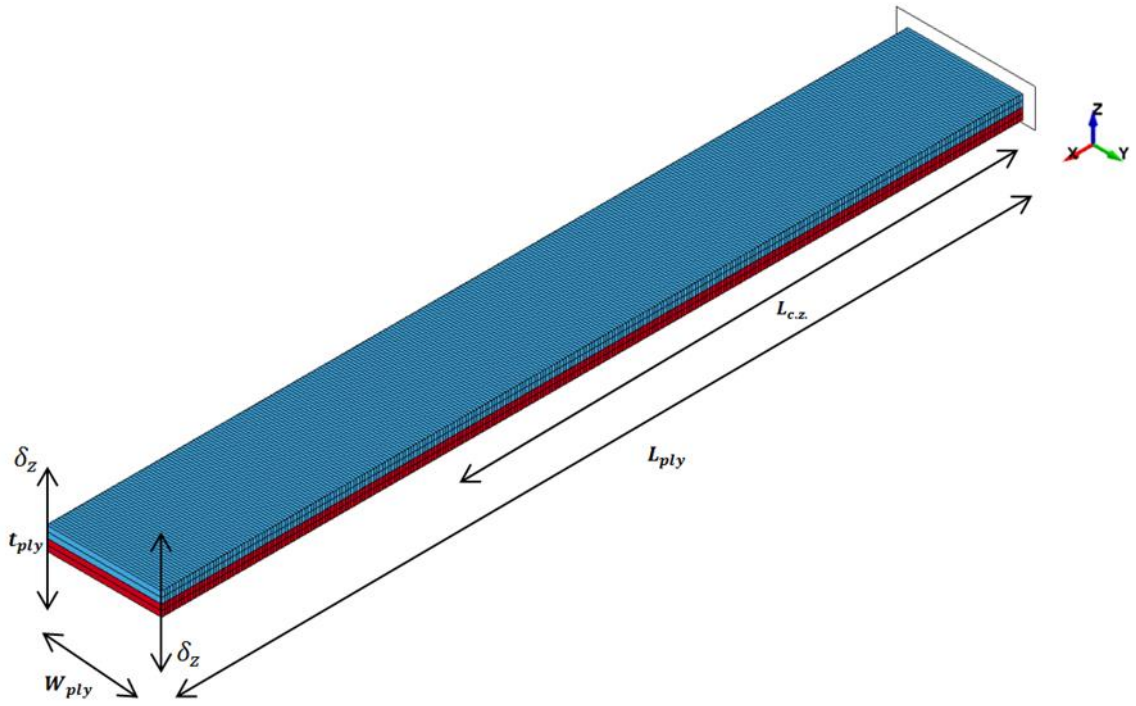


**Figure 3.5 -** Test specimen modeled in LS-DYNA

As for the material of the plies, a simple orthotropic elastic material is chosen – *MAT_ORTHOTROPIC_ELASTIC (*MAT_002). The definition of this material and the ones that will be described next are shown in the Appendix. Table 3.1 and Table 3.2 represent the dimensions of the test specimen and the mechanical and interface material properties of the plies and the cohesive element properties [40], respectively.

**Table 3.1 -** Dimensions of the test specimen

| $W_{ply}$ $(mm)$ | $L_{ply}$ $(mm)$ | $L_{c.z.}$ $(mm)$ | $t_{ply}$ $(mm)$ | $t_{c.e.}$ $(mm)$ |
|---|---|---|---|---|
| 20.000 | 150.000 | 95.000 | 1.980 | 0.100 |

**Table 3.2 -** Material properties of the plies and the cohesive elements taken from [40]

| $E_{11}$ $[GPa]$ | $E_{22} = E_{33}$ $[GPa]$ | $G_{12} = G_{13}$ $[GPa]$ | $G_{23}$ $[GPa]$ |
|---|---|---|---|
| 150.00 | 11.00 | 6.00 | 3.70 |
| $v_{12} = v_{13}$ | $v_{23}$ | $G_{IC}$ $[N/mm]$ | $\tau_3^0 = T$ $[MPa]$ |
| 0.25 | 0.45 | 0.35 | 60.00 |

As mentioned before, when modeling in LS-DYNA, the user must define the following Poison's ratios: $v_{ba} = v_{21}$, $v_{ca} = v_{31}$ and $v_{cb} = v_{32}$. From equation 2.2:

$$\begin{cases} v_{21} = v_{31} = 0.18(3) \\ v_{32} = v_{23} = 0.45 \end{cases}$$

Using *MAT_138 as the material card for the cohesive elements, two more parameters must be defined. These correspond to the interface stiffness normal to the plane and in the plane of the cohesive element ($EN$ and $ET$, respectively). Alternatively, the ultimate displacement in the normal and in the tangential direction, which are the displacement at the time when the material has failed completely, i.e., the tractions are zero, can be specified instead of the peak tractions ($T$ and $S$). In [40] it is stated that for a sub-laminated thickness between 0.125 mm and 5 mm, the range of the interface stiffness $K$ must be between $10^5$ and $5\times10^6 N/mm$. In the present dissertation, the interfacial stiffness is $K = EN = 10^6 N/mm$. The ultimate displacement in the normal direction is obtained by the following equation 3.3, [37], and the properties of the material of the cohesive elements are presented in Table 3.3.

$$\delta_n^c = UND = \frac{2 \times G_{IC}}{T} \tag{3.3}$$

**Table 3.3 -** Final properties of the material of the cohesive elements

| $EN = ET$ $[N/mm^3]$ | $G_{IC} = G_{IIC}$ $[N/mm]$ | $T = S$ $[MPa]$ | $XMU$ |
|---|---|---|---|
| $10^6$ | 0.352 | 60 | -1.5 |

The section of the elements must be defined as well as the contact between the plies, due to volume interferences between the different unidirectional plies [43]. As stated before, regarding the section of the plies, for the solid elements the element formulation chosen is 2, which is a fully integrated selective reduced (S/R) solid. For the thick-shell elements, the element formulation chosen is 5, which is an assumed strain reduced integration, and the formulation 19 is chosen for the cohesive elements, which is a four-point cohesive element. For the contact, Eroding contact types are recommended whenever solid elements involved in the contact definition are subject to erosion (element deletion) due to material failure criteria, being the card *Contact_Eroding_Single_Surface [43] the chosen contact. These eroding contacts contain logic which allow the contact surface to be updated as exterior elements are deleted [44]. Finally, for the hourglass control, the option 2 is chosen, which refers to the Flanagan-Belytschko viscous form. After implementing both models the simulations are carried out, being the delaminated test specimen represented in Figure 3.6.

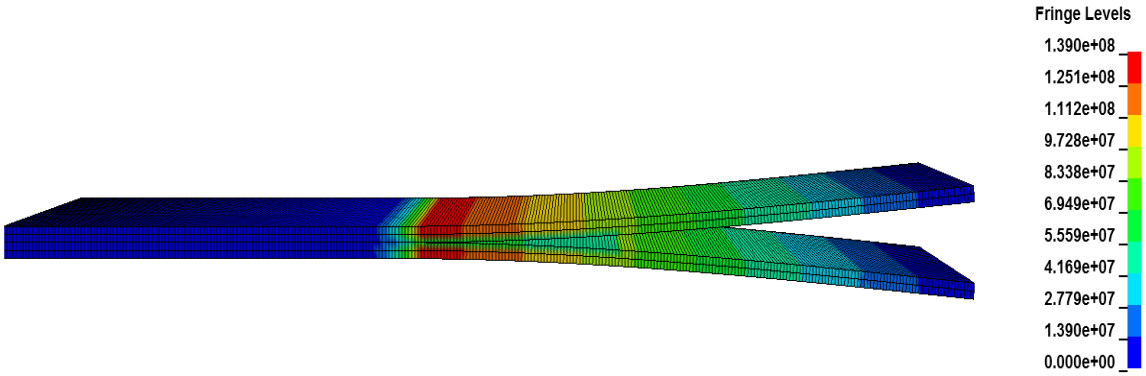


**Figure 3.6 -** Test specimen after delamination – VM Stress [Pa]

Figure 3.7 shows the curves obtained with solid and thick-shell elements in LS-DYNA and the experimental curve from [40].

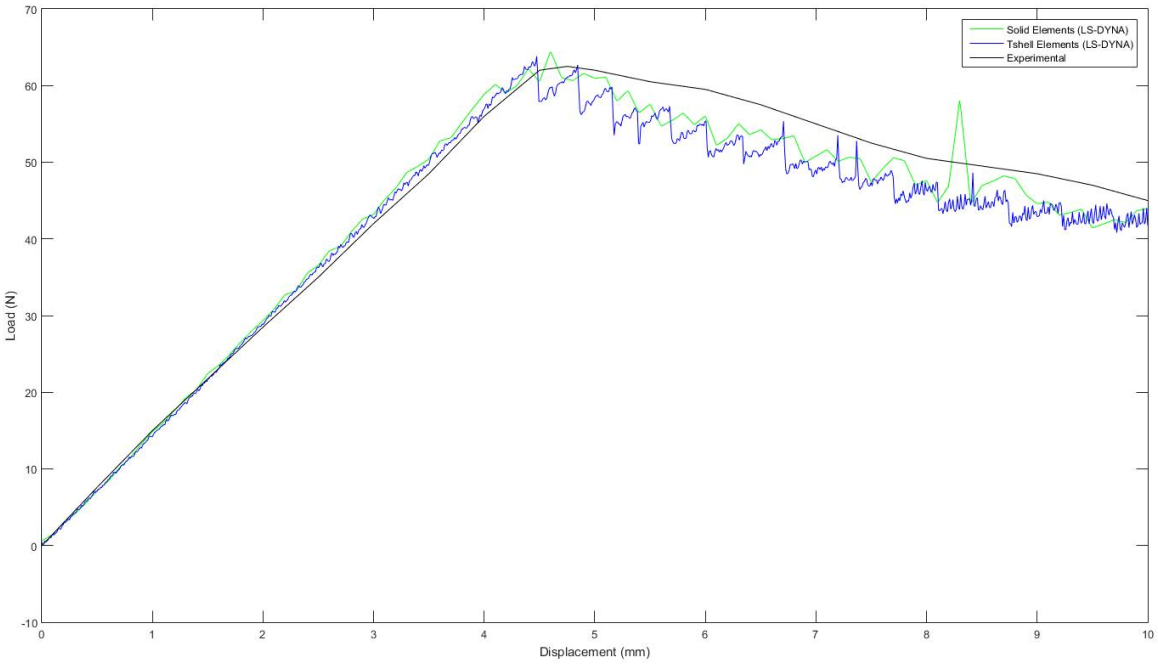


**Figure 3.7 -** Load-Displacement curves - comparison between LS-DYNA simulations and experimental data

It is also important to validate the LS-DYNA model with the one developed by Mangualde in ANSYS [39]. In order to do it, in Figure 3.8 is depicted the comparison between both numerical models, as well as the experimental curve.

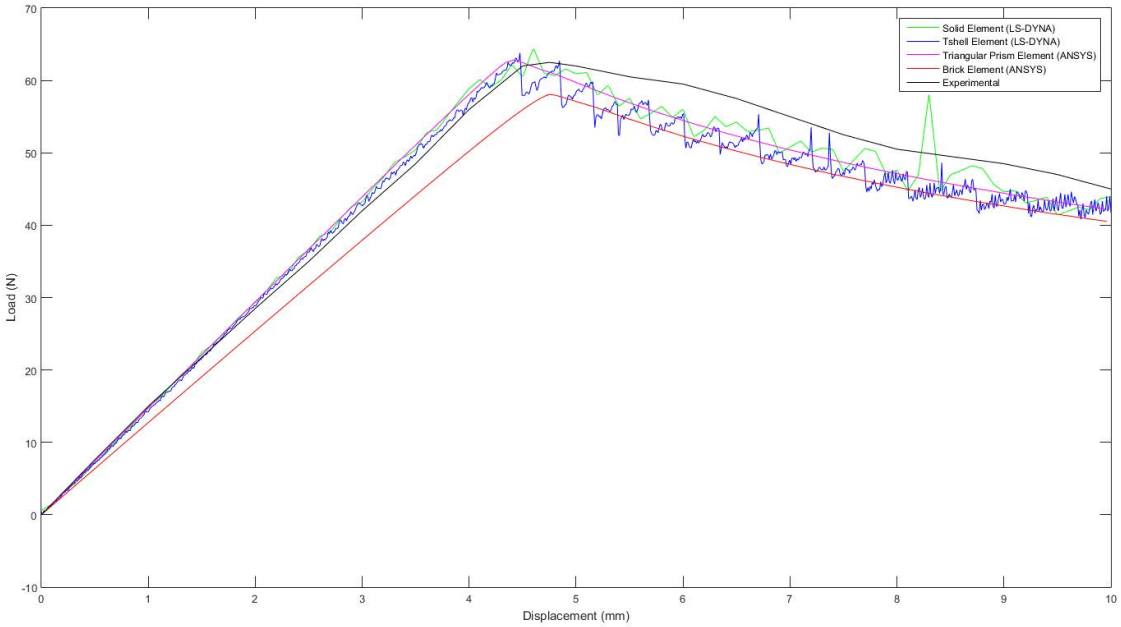


**Figure 3.8 -** Load-Displacement curves - comparison between LS-DYNA and ANSYS numerical simulations and experimental data

As expected, observing the curves we can verify that the results obtained from the numerical simulations have a good match between them, as well as with the experimental results. Even more, as it is possible to observe, despite the spikes verified in the curves taken from LS-DYNA, which could be explained by the elements that fail and that are then deleted causing the force to drop in that exact instance (also could be due to hourglass or some element distortion), it can be concluded that the numerical models response is very much alike. Another LS-DYNA model was also tested using element formulation 1 due to its low computational cost, however it was detected element distortion and so element formulation 2 is maintained. Although other types of hourglass and element formulation could be tested, for now it can be concluded that both LS-DYNA numerical models for the delamination are identified and ready to be applied in the next step.

## 3.2 Combined Failure Criterion

As mentioned in chapter two, failure criteria predicts the stress and strain values for which the material fails when subject to the action of external loads.

In order to validate the tests developed in this dissertation with the ones developed in Mangualde's dissertation, the failure criteria that will be used must be the same or equivalent. Given both dissertations are a continuation of the one developed by Crespo [2], the failure criteria that is used is a combination of the maximum stress failure criterion and the Tsai-Wu failure criterion.

The maximum stress failure criterion demonstrates the failure occurring when the principal stress exceeds a specific value, but, as one of the goals of this work is to develop methodologies capable of predicting the behaviour of composites with different layups, other directions besides the principal directions must be taken into account. Precisely for that reason, the Tsai-Wu failure criterion is the chosen second criterion, mainly since it's one of the most used criteria to predict material failure and is extensively used in determining the damage initiation of a ply. However one of the drawbacks of this criterion is the fact that the failure stress of the fiber in a lamina exceeds the strength of the material for the case of symmetric angle-ply laminates with small fiber angles subjected to off-axis tension [45]. These criteria complement themselves and in order to eliminate the drawbacks between both, Crespo decided to use a combination of the two, which will also be used in this dissertation.

In the study developed by Lin and Hu [45], this combined failure criterion, for the plane stress condition, is demonstrated as the following:

$$\sigma_1/X_T \leq 1 \quad \text{or} \quad \sigma_1/X_C \leq 1 \tag{3.4}$$

and

$$F_1\sigma_1 + F_2\sigma_2 + F_{11}\sigma_1^2 + F_{22}\sigma_2^2 + F_{66}\sigma_{12}^2 < 1 \tag{3.5}$$

The Figure 3.9 represents the stress state permissible area of the material when using the combination of both failure criteria.

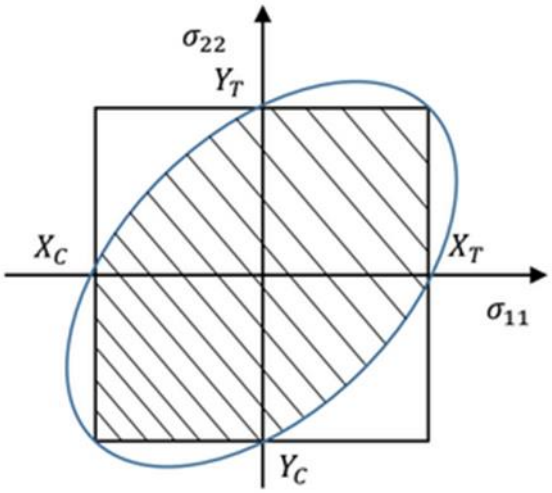


**Figure 3.9 -** Combination of the maximum stress (represented in black) and the Tsai-Wu (represented in blue) failure criteria [2]

### 3.2.1 Implementation of the Combined Failure Criterion in LS-DYNA

Here is described how the combined failure criterion is implemented. A study of the LS-DYNA volume II [37] was carried out and so far there is no orthotropic material implemented in this software that allows the use of both failure criteria for the same material. In order to use both criteria, two material cards are chosen, *MAT_ENHANCED_COMPOSITE_DAMAGE (*MAT_55), which allows the implementation of the Tsai-Wu failure criterion, and *MAT_ADD_EROSION, which allows the implementation of the maximum stress failure criterion. *MAT_ADD_EROSION is a very simple material card that allows the implementation of failure and erosion in material models [37]. In this card the variable SIGP1 represents the principal stress at failure $\sigma_{max}$, which allows the use of the maximum stress failure criterion and in this input the value of $X_T$ or $X_C$ is established, depending on whether the test is a tensile or compression test, respectively. However, this card has one drawback for thick shells, because only element formulations 1 and 2 are admissible. For this

reason, from now on, only 8-node hexahedron solid elements will be used in the remaining numerical models.

*MAT_55 card has implemented the Tsai-Wu failure criterion and the Chang Chang failure criterion [37]. Five inputs of this card must be established for the failure criteria, $X_T$, $X_C$, $Y_T$, $Y_C$ and $S_L$. The longitudinal tensile and compressive strength ($X_T$ or $X_C$, respectively) and the shear strength ($S_L$) are used in the Chang Chang failure criterion to obtain the failure for the tensile fiber mode

$$\sigma_{aa} > 0 \Rightarrow e_f^2 = \left(\frac{\sigma_{aa}}{X_T}\right)^2 + \beta\left(\frac{\sigma_{ab}}{S_L}\right) - 1 \begin{cases} \geq 0 & failed \\ < 0 & elastic \end{cases}, \tag{3.6}$$

$$E_a = E_b = G_{ab} = v_{ba} = v_{ab} = 0$$

and compressive fiber mode

$$\sigma_{aa} < 0 \Rightarrow e_c^2 = \left(\frac{\sigma_{aa}}{X_C}\right)^2 - 1 \begin{cases} \geq 0 & failed \\ < 0 & elastic \end{cases}, \tag{3.7}$$

$$E_a = v_{ba} = v_{ab} = 0$$

The transverse tensile and compressive strength and the shear strength ($Y_T$, $Y_C$ and $S_L$, respectively) are used in the Tsai-Wu failure criterion to obtain the failure for the tensile and compressive matrix mode,

$$e_{md}^2 = \frac{\sigma_{bb}^2}{Y_C Y_T} + \left(\frac{\sigma_{ab}}{S_L}\right)^2 + \frac{(Y_C - Y_T)\sigma_{bb}}{Y_C Y_T} - 1 \begin{cases} \geq 0 & failed \\ < 0 & elastic \end{cases}, \tag{3.8}$$

Therefore, in order to implement the combined failure criterion, when establishing the values for the failure tensions, the value of $X_T$ and $X_C$ is scaled by $10^2$ in *MAT_55. This way, when applying tensile or compressive strengths, the test specimen will either fail by the maximum stress or the Tsai-Wu failure criterion and never by the Chang Chang criterion.

### 3.2.2 Simulation Analysis and Results

After deciding which criteria to use and how to implement them, a model of one ply with the same type of contact previously referenced and no cohesive elements was created in order to compare it with the simulation of the damage propagation of the ANSYS numerical model, with the model depicted in Figure 3.10. The mesh (nodes and elements) is generated by a in-house MATLAB routine called "Mesh Generation Algorithm" developed by Mangualde [4], with some modifications in order for it to work on LS-DYNA.

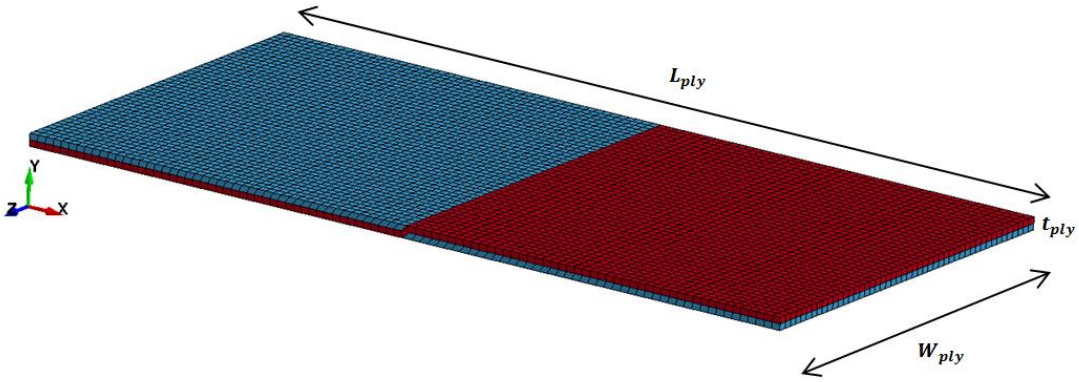


**Figure 3.10 -** Test specimen generated by the Mesh generation algorithm

In Table 3.4 are depicted the spread tow carbon fabric ply dimensions, being the constants of the orthotropic material of the ply presented in Table 3.5 [46].

**Table 3.4 -** Dimensions of the spread tow carbon fabric ply

| $W_{ply}$ $(mm)$ | $L_{ply}$ $(mm)$ | $t_{ply}$ $(mm)$ |
|---|---|---|
| 10.05 | 20.01 | 0.304 |

**Table 3.5 -** Material properties of the spread tow carbon fabric ply [46]

| $E_{11}$ $[GPa]$ | $E_{22}$ $[GPa]$ | $E_{33}$ $[GPa]$ | $v_{12}$ | $v_{23}$ | $v_{13}$ | $G_{12}$ $[MPa]$ | $G_{13}$ $[MPa]$ | $G_{23}$ $[MPa]$ |
|---|---|---|---|---|---|---|---|---|
| 161 | 11.38 | 11.38 | 0.32 | 0.32 | 0.436 | 5170 | 5170 | 3980 |

For this model in particular the constants provided by the five uniaxial tests are the ones previously used by Crespo [2] that were extracted from Maimí [23], and are shown in Table 3.6:

**Table 3.6 -** Failure tensions provided by the five uniaxial tests [1,21]

| $X_T$ $[MPa]$ | $X_C$ $[MPa]$ | $Y_T$ $[MPa]$ | $Y_C$ $[MPa]$ | $S_L$ $[MPa]$ |
|---|---|---|---|---|
| 500 | 350 | 62.3 | 199.8 | 92.3 |

The model is represented in Figure 3.11, with the respective boundary condition that are applied on one of the ends of the ply. On the other end, a displacement of 0.11 mm is imposed.

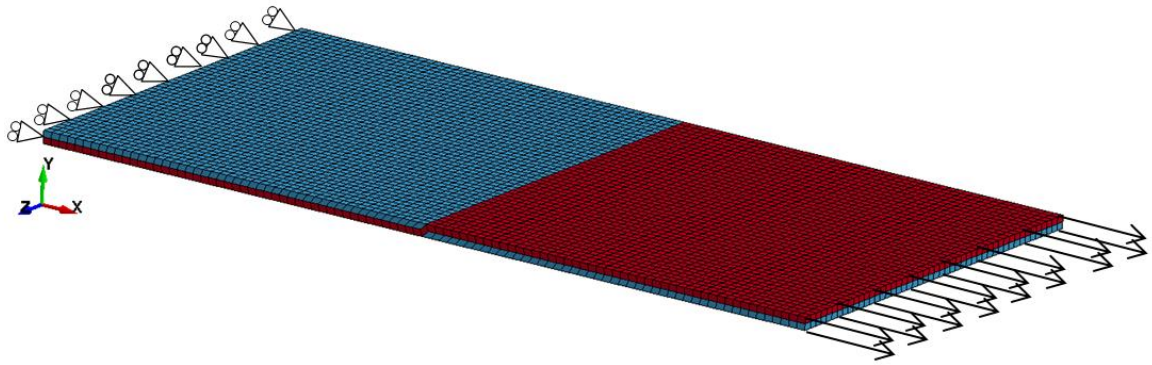


**Figure 3.11 -** Test specimen with respetive boundary conditions

Regarding the section of the elements, element formulation -1 is chosen. This is an accurate formulation of fully integrated S/R solid intended for elements with poor aspect ratio. This formulation is chosen due to only having one element along the thickness and when using element formulation 2 the phenomenon known as shear lock would occur. With the model prepared, when running the simulation, the computational time is too high and counterproductive to the objectives established for this dissertation. In order to solve this problem a scale factor is applied in the termination time, establishing a time of 1 second to 1 millisecond. This means that the velocity is greatly increased, because for the same displacement of 0.11mm the loading time is significantly reduced. However, this solution induces error in the result of the simulation. To prevent this from happening, the card *CONTROL_TIMESPET is implemented. This card allows to input a value for the variable TSSFAC between 0.67 and 0.4, which represents a scale factor for the computed time and prevents distortions of these elements. This card will be used for all the models presented from this moment on.In Figure 3.12 and Figure 3.13 the results of the damage propagation of the material are represented.

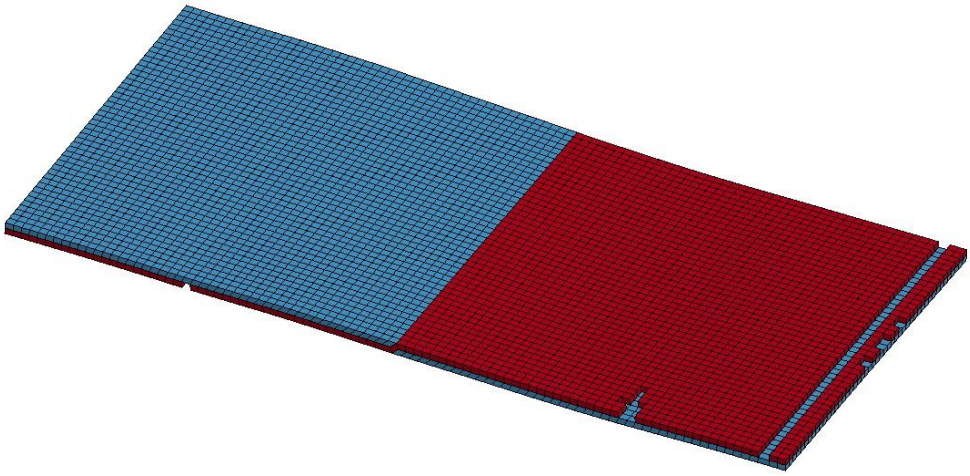

**Figure 3.12 –** Damage propagation of the test specimen

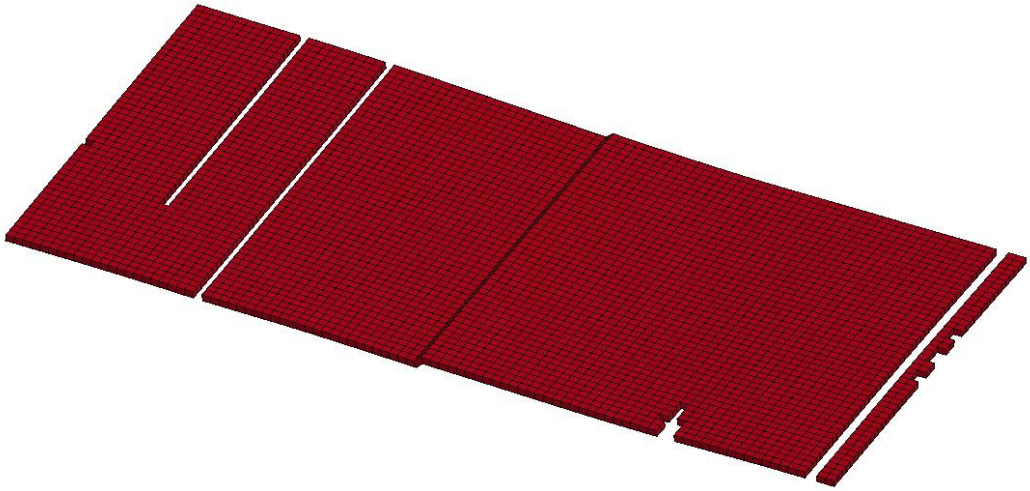

**Figure 3.13 -** Illustration of all the failed elements of the 0º ply

As it can be seen, the elements that fail are the ones that constitute the fibers aligned in the xx direction (0º fibers) while the ones aligned with the *z*-direction show no failure for the imposed displacement. As it was expected fiber failure occurred first than matrix failure, which means that the elements failed by the maximum stress failure criteria. These might have occurred since these fibers are aligned with the displacement imposed and, therefore, these are the ones that support much of the tensions present in the ply. However, the area where the elements are expected to fail is in the warp/weft transition. This might not have occurred due to the eight failed integration points prior to element deletion that are implemented in *MAT_ADD_EROSION, which make the system more conservative.

Figure 3.14 shows the force-displacement diagram obtained from this simulation. Observing the curve, it can be seen a pick force around 812 N followed by a drop due to the failure of the first elements in the fibers aligned with the *x*-direction. After this failure, the force continues to increase and decrease, due to some elements that are eliminated, until the displacement of 0.11 mm is reached.

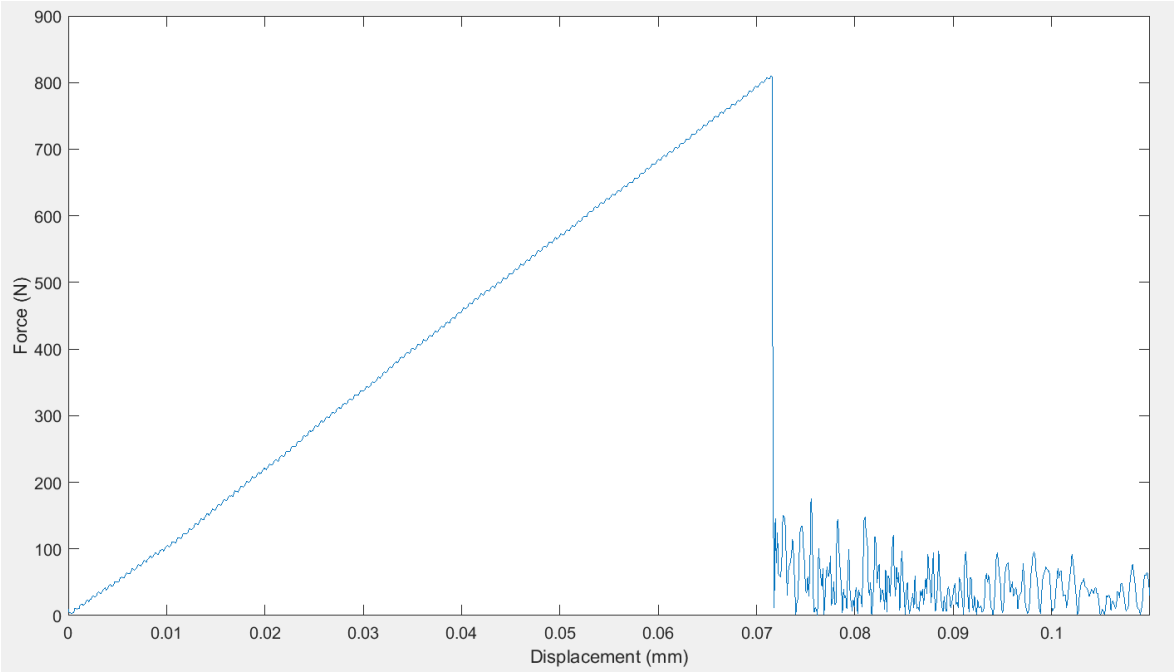


**Figure 3.14 -** Force vs Displacement curve obtained from the LS-DYNA model simulation

The damage propagation of the material of the ANSYS numerical model represented in Figure 3.15 is very similar. The elements that fail are also the ones in the fibers aligned with the *x*-direction and also in the same zone of the ply, although the number of elements that fail is greater than the number obtained in the simulation ran in LS-DYNA. This difference might be explained by the different solvers (LS-DYNA and ANSYS/MATLAB), and the different step sizes imposed in ANSYS model, during the implicit static analysis, and the LS-DYNA model, during the explicit dynamic analysis.

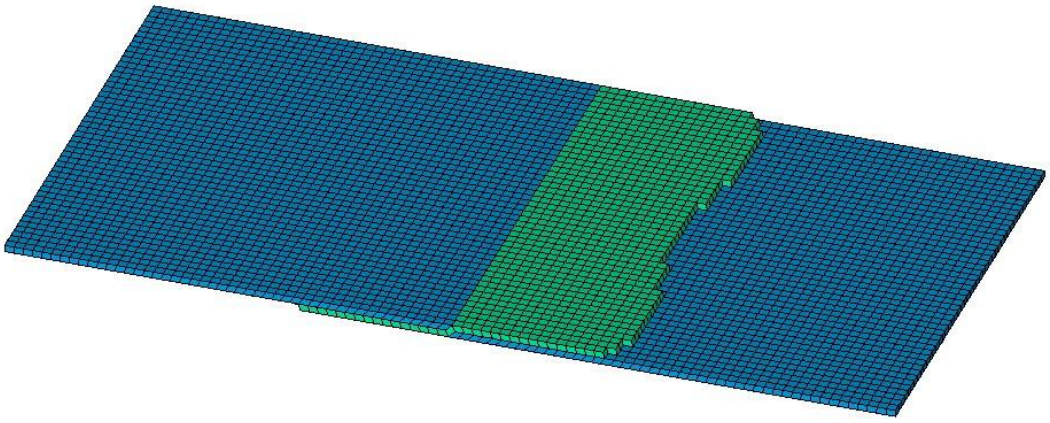

**Figure 3.15 -** Damage propagation of Mangualde's test specimen [4]

Finally, in Figure 3.16 is presented the force-displacement diagram resultant from Mangualde's simulation, showing a pick force of 810 N, followed by a drop due to failure of the elements of the fibers aligned with the *x*-direction. The results obtained from both simulations show a relative difference around 2% which is a very good accuracy given the different solvers used and thus the models are validated.

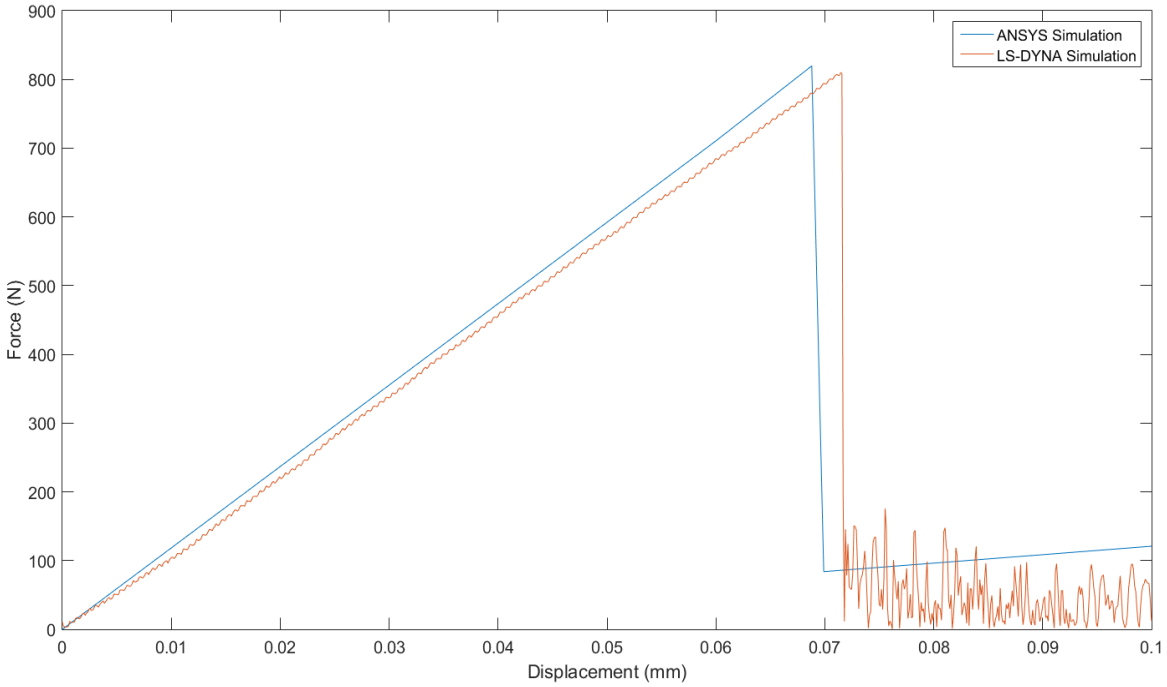


**Figure 3.16 -** Comparison between the Force vs Displacement curves obtain in ANSYS and LS-DYNA

# 4
# Numerical Analysis of Models of CFRP Test Specimens

After the study and respective validation of the cohesive elements and the combined failure criterion models, more detailed and serious tests are conducted and described in this chapter. Initially three studies are made in order to observe the behavior of one ply with 0°/90°, 15°/75° and 30°/60° arrangement. For each study, two tests are conducted where one does not have any cohesive properties between the warp and the weft and are tied by the nodes these two share, i.e., the warp and the weft share the same node at their interface, and the second model does have cohesive properties by implementing a cohesive contact, in order to observe the delamination between the warp and the weft. The objective is to observe the difference in the test specimen's behavior when subjected to external loads and compare the results with the ones obtained by Mangualde [4]. Upon this study, two models of a test specimen of ten and twenty-six plies subjected to tensile and compressive loads, respectively, will be tested and the results will be compared with the ones obtained with ANSYS/MATLAB models.

A MATLAB routine developed by Mangualde, [4], to generate the APDL file [4,39], for the test specimens was modified in order to write a mesh (nodes and elements) in a form of a Keyword (LS-DYNA input) file. The routine is very similar to the one used in the previous chapter to generate one ply. It allows the user to choose the size of the element and the number of plies, however the main feature of this program is the transitional cell randomness, i.e., in any given ply, the change of cell can appear anywhere along its length.

## 4.1 Numerical model of a test specimen with a 0°/90° arrangement

Although in the previous chapter the delamination was studied using cohesive elements, , due to the complexity in the geometry of the transitional cells and the computational cost inherent to the increasing number of elements, a cohesive contact between the elements aligned in 0° and 90° is implemented. Studies show that this alternative is simpler than the CZM approach. Although not as accurate, this method is effective to predict the delamination.

Figure 4.1 represents the test specimen which is very similar to the one represented in Figure 3.10. However, some modifications, in regard to that previous model, were made. In order to compare the results with Mangualde a less conservative model is needed. With that in consideration a more refined mesh was implemented in the test specimen and with that only one failed integration point prior to element deletion, instead of the 8 failed points previously used, was considered. The boundary conditions are the same as the ones implemented in the model in chapter 3.2.2: one end of the specimen fixed in the *x*-direction and in the other end with an imposed displacement of 0.11 mm in the *x*-direction.

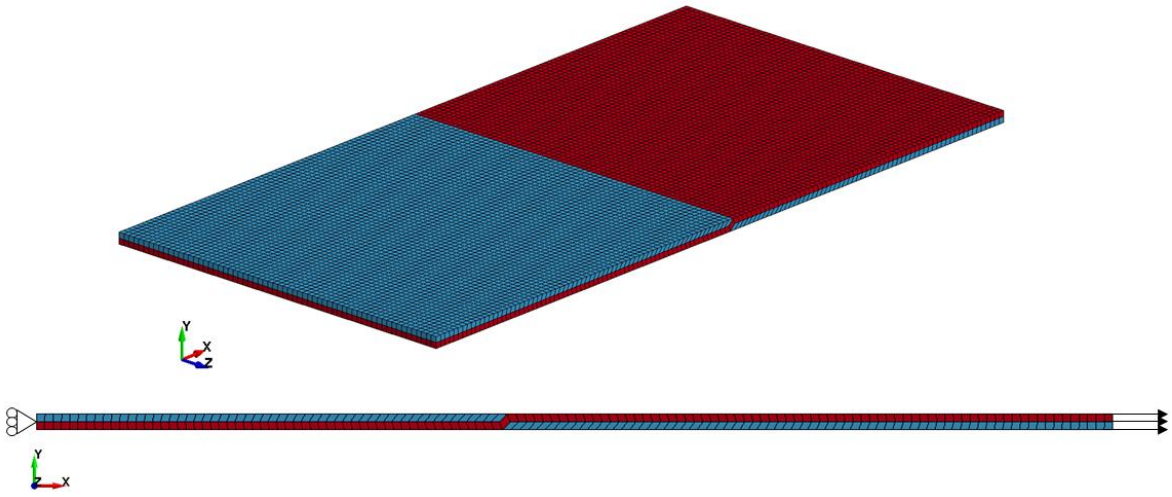

**Figure 4.1-** Representation of the test specimen with 0°/90° arrangement and respective boundary conditions

The properties of the material of the plies are the same as the ones presented in the chapter 3.2.2 in Table 3.5, however the cohesive properties are different. In the chapter 3.1.1, cohesive properties were taken from Camanho's paper [40], where mode I delamination was predominant. However, in order to study the mix mode behavior the new properties, presented in Table 4.1, are taken from Kawashita's paper [46], the same used to take the material properties of the plies.

**Table 4.1-** Properties for the cohesive contact taken from [46]

| $EN$ $[N/mm^3]$ | $ET$ $[N/mm^3]$ | $G_{IC}$ $[N/mm]$ | $G_{IIC}$ $[N/mm]$ | $T$ $[MPa]$ | $S$ $[MPa]$ |
|---|---|---|---|---|---|
| $10^6$ | $10^6$ | 0.2 | 1.0 | 60 | 90 |

In order to simulate the cohesive contact between the warp and weft, the following card is chosen: *CONTACT_AUTOMATIC_ONE_WAY_SURFACE_TO_SUFACE_TIEBREAK. This card has many options that allow the implementation of different formulations in order to predict delamination. Given that in the previous study of delamination for the cohesive element the material *MAT_138 was chosen, for the card of the cohesive contact is selected option 9, because the input variables for this option correspond to the input variables in *MAT_138, which are presented in Table 4.2.

**Table 4.2-** Relation between the input variables of the cohesive contact option 9 and the material *MAT_138

| **Contact** | ***MAT_138** |
|---|---|
| NFLS | T |
| SFLS | S |
| PARAM | XMU |
| ERATEN | $G_{IC}$ |
| ERATES | $G_{IIC}$ |
| CT2CN | ET/EN |
| CN | EN |

Regarding the section of the elements, element formulation -1 is used. This is an accurate formulation of fully integrated S/R solid intended for elements with poor aspect ratio. This formulation is preferred to avoid element distortion, observed in the simulation when the element formulation 1 was

implemented, and shear locking, which occurs when using element formulation 2. It should be noted that, despite using a fully integrated solid element, only one failed integration point prior to failure is implemented.

After implementing the features analyzed in the previous chapter and the new ones previously described in the model, the simulation is carried out. Figure 4.2, Figure 4.3 and Figure 4.4 represent both final stages of the simulations with and without cohesive contact between the warp and weft, and the force-displacement curve for both simulations, respectively.

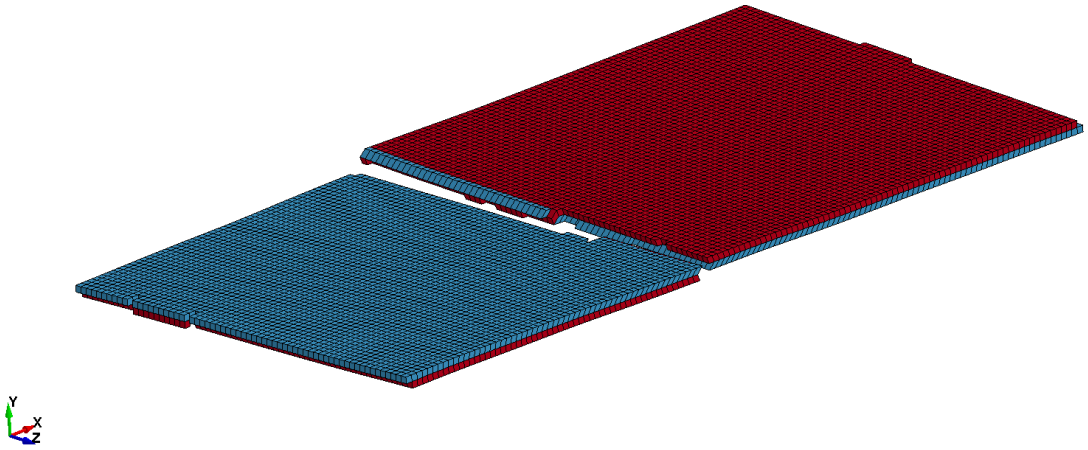


**Figure 4.2-** Final stage for the test specimen with 0°/90° arrangement with cohesive contact

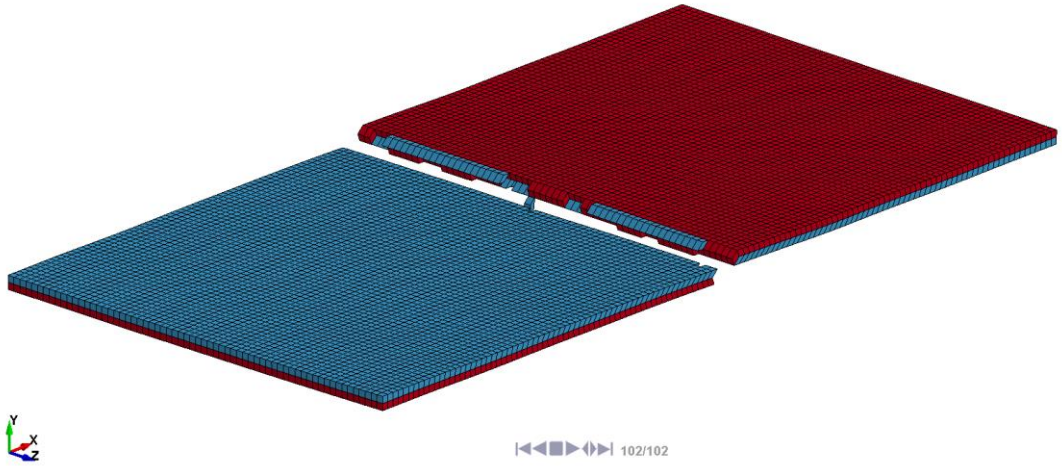


**Figure 4.3-** Final stage for the test specimen with 0°/90° arrangement without cohesive contact

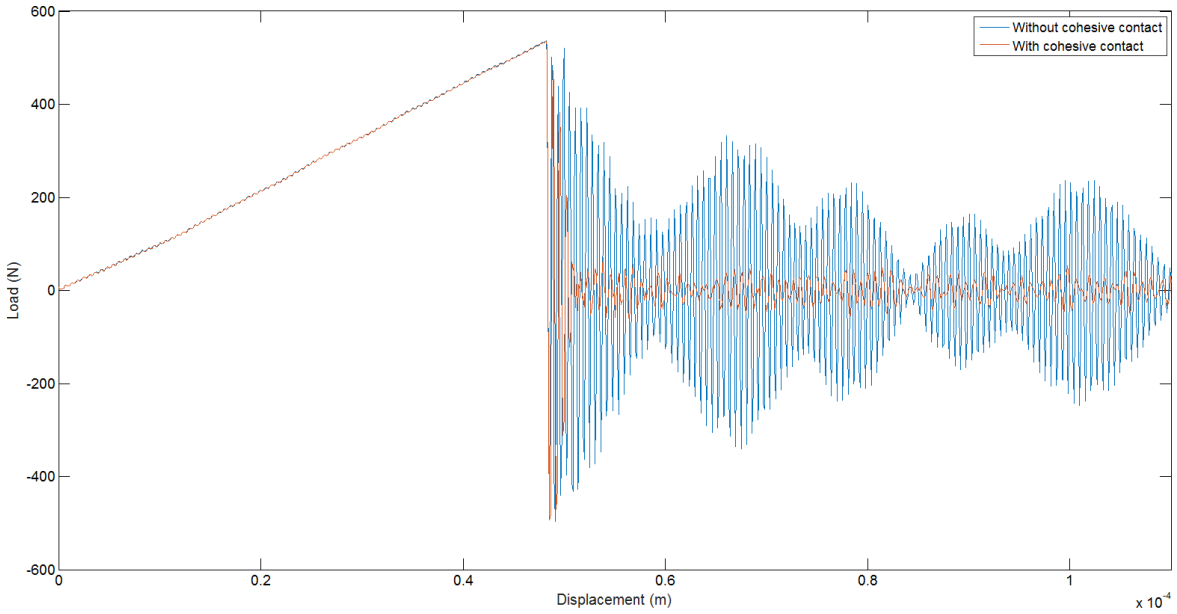


**Figure 4.4-** Comparison between the Force vs Displacement curves for both 0°/90° models

Observing the final stages for both models, contrary to what was observed in Chapter 3.2.2, failure occurs in the area of the warp/weft transition, which is the expected result in the first place, due to the fact that the stress concentration is critical in this area. It can be concluded that a fully integrated solid does not always lead to better results, for only using one failure integration point instead of eight, which is used in the combined failure criterion, yielded the expected behavior as the ply that was tested experimentally. Finally, observing the force displacement curve, both simulations resulted in the same pick of force right before failure occurred, with a value of 536 N.

It can be concluded that for this model, using cohesive contact between the warp and the weft does not significantly affect the behavior of the ply, nor the load necessary for its failure.

Observing the results described in Mangualde's dissertation [4], for the same test specimen, failure of the elements occurred in the same area as the ones presented in this section. As for the force-displacement curves, a comparison between the results obtained in LS-DYNA and the ones obtained in ANSYS is represented in Figure 4.5.

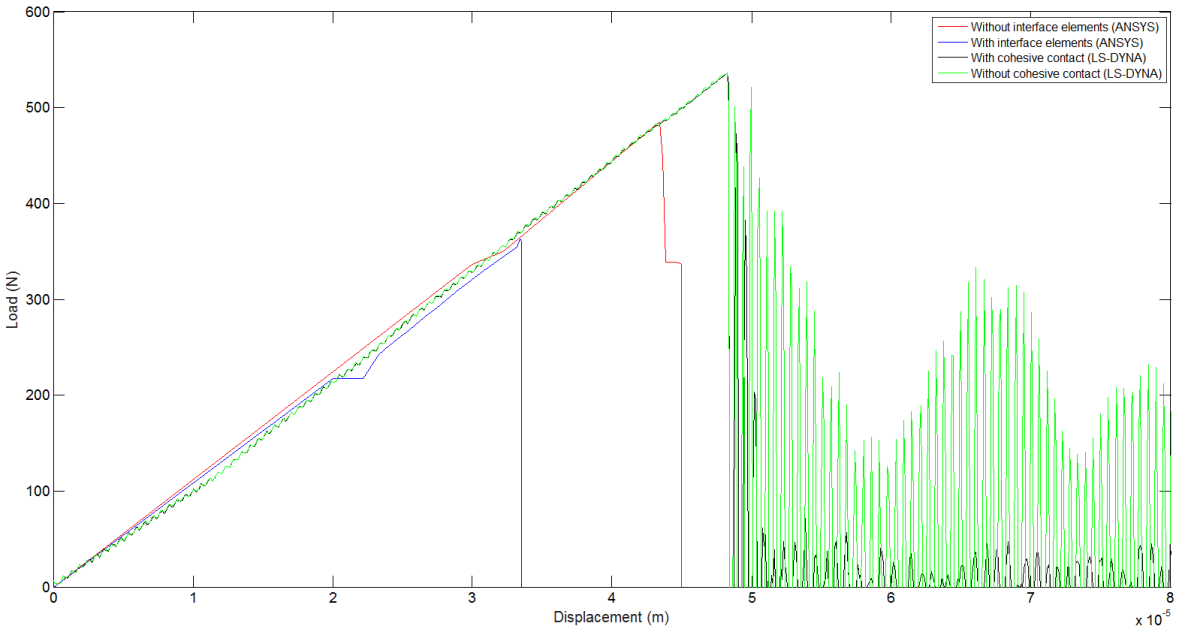


**Figure 4.5-** Comparison between the results obtained in LS-DYNA and ANSYS for the 0º/90º model

Observing the curves, the difference between the results of the models without cohesive contact and interface elements is around 9%, with the result in Mangualde's simulation achieving a pick force of 484 N, while the difference between the other two curves is around 30%, with Mangualde's simulation showing a pick force of around 375 N. The models without cohesive properties show a good correlation, however the difference of results of the other two models was not expected. Nonetheless, the difference of results between the ANSYS numerical models was not expected (around 28%), and could explain the difference in the results of the models with cohesive properties between the warp and the weft.

## 4.2 Numerical model of a test specimen with a 15°/-75° arrangement

Contrary to the model with a 0°/90° arrangement, where an elastic behavior is acceptable, this model, and the two that are studied next, are expected to have a plastic behavior, according to experimental results, as the ones shown in Figure 1.1. However due to the computational cost and the complexity inherent to the modeling of plastic behavior, in the present study, for this model and the one that will be conducted next, only an elastic behavior will be considered. Figure 4.6 represents the test specimen with a detail showing, for each element, the local coordinate system with 15°/-75° arrangement. As it can be seen the area of the change of cell is not parallel to the width of the ply like in the 0º/90º arrangement. However, this is not enough to define the orientation of the ply and so, using "Element Editing → Direction", a local coordinate system can be implemented for each element of the model.

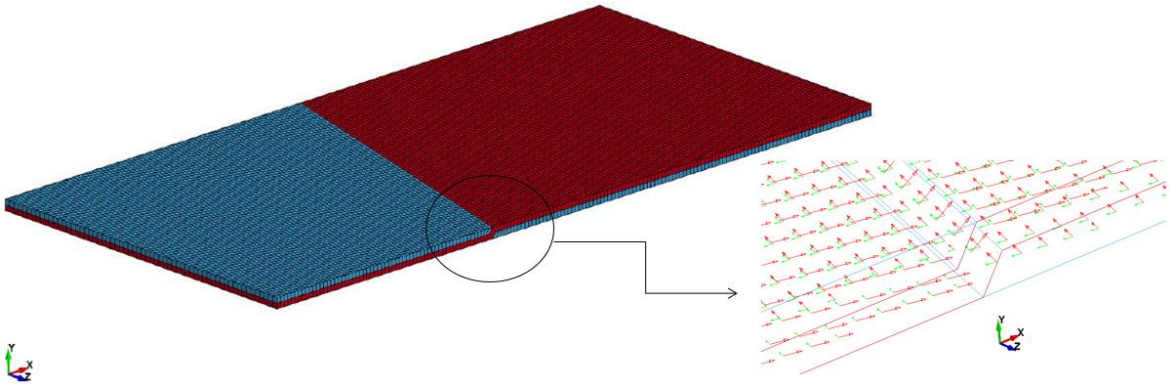

**Figure 4.6 -** Test specimen with a 15º/-75º arrangement and a detail showing the local coordinate system for the elements in and near the transition

The boundary conditions, material properties, cohesive properties and sections are the same used in the previous model. After implementing all the features in the model, the simulation is carried out. Figure 4.7, Figure 4.8 and Figure 4.9 represent both final stages of the simulations with and without cohesive contact between the warp and weft, and the force-displacement curve.

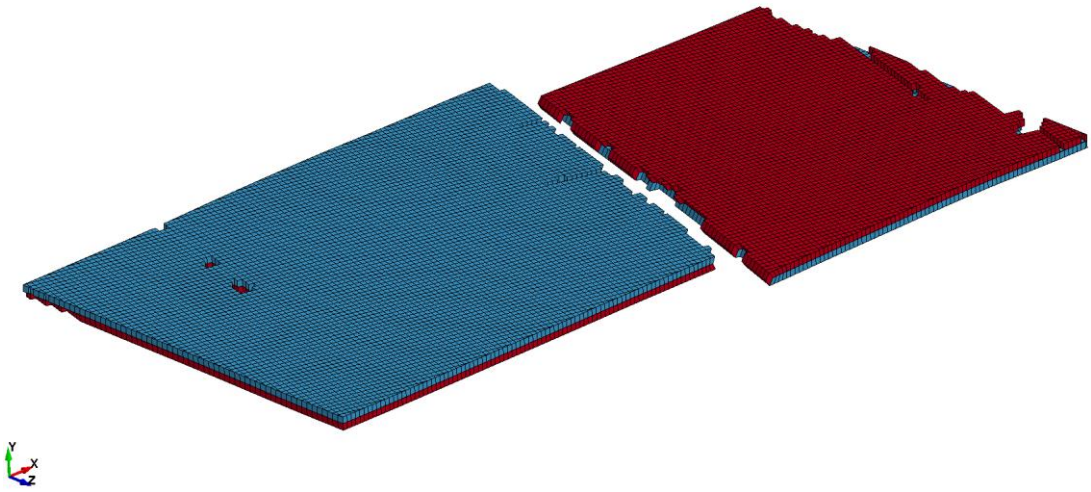

**Figure 4.7-** Final stage for the test specimen with 15°/-75° arrangement with cohesive contact

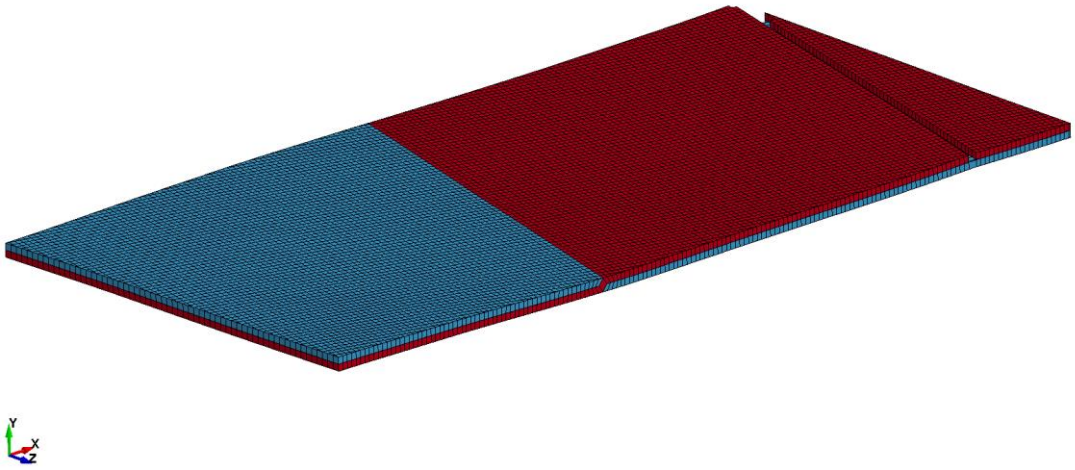

**Figure 4.8-** Final stage for the test specimen with 15°/-75° arrangement without cohesive contact

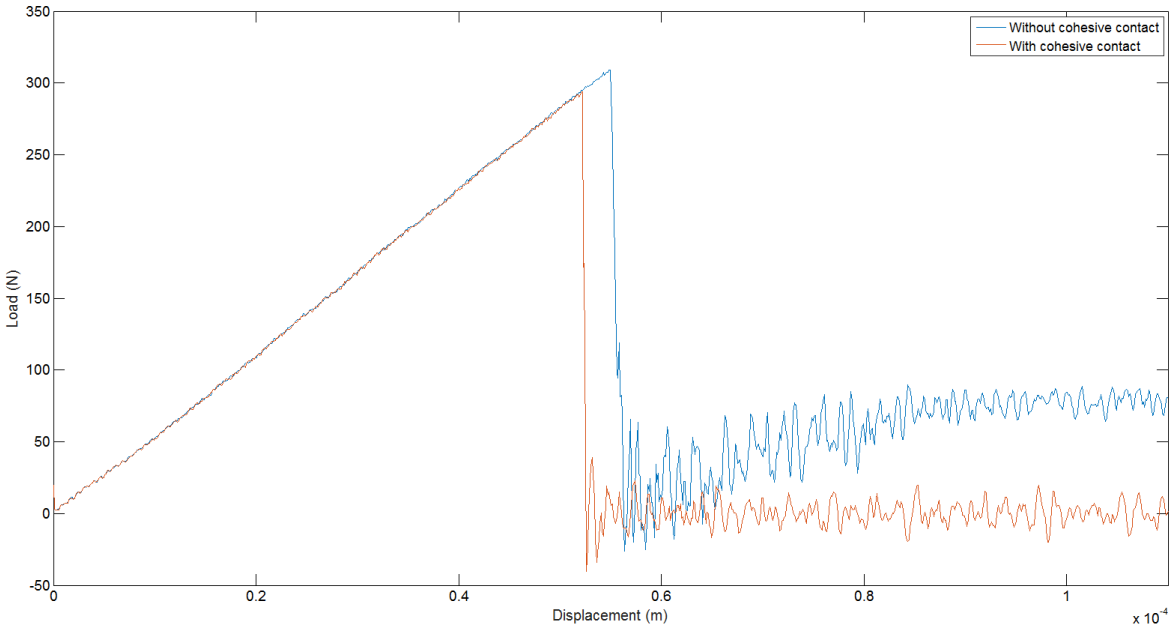


**Figure 4.9-** Comparison between the Force vs Displacement curves for both 15°/-75° models

Contrary to what happened in the previous section, both models have different behaviors. In the model where cohesive contact is implemented, failure occurs as expected in the warp/weft transition, with the interesting fact that the cut is not as "clean" as the one observed in the model with a 0°/90° arrangement, while in the model without cohesive contact failure occurs between the warp/weft transition and the area where the displacement is imposed.

For both simulations, the force-displacement curve resulted in a very similar pick of force of 295 N for the model with cohesive contact and 309 N for the model without, with a difference of about 5% Thus can be concluded that, for this model, using cohesive contact between the warp and the weft does not affect significantly the load necessary to produce failure, however it affects the behavior of the ply when subjected to external forces.

In Figure 4.10 the comparison between the results obtained in LS-DYNA and the ones obtained in ANSYS is represented.

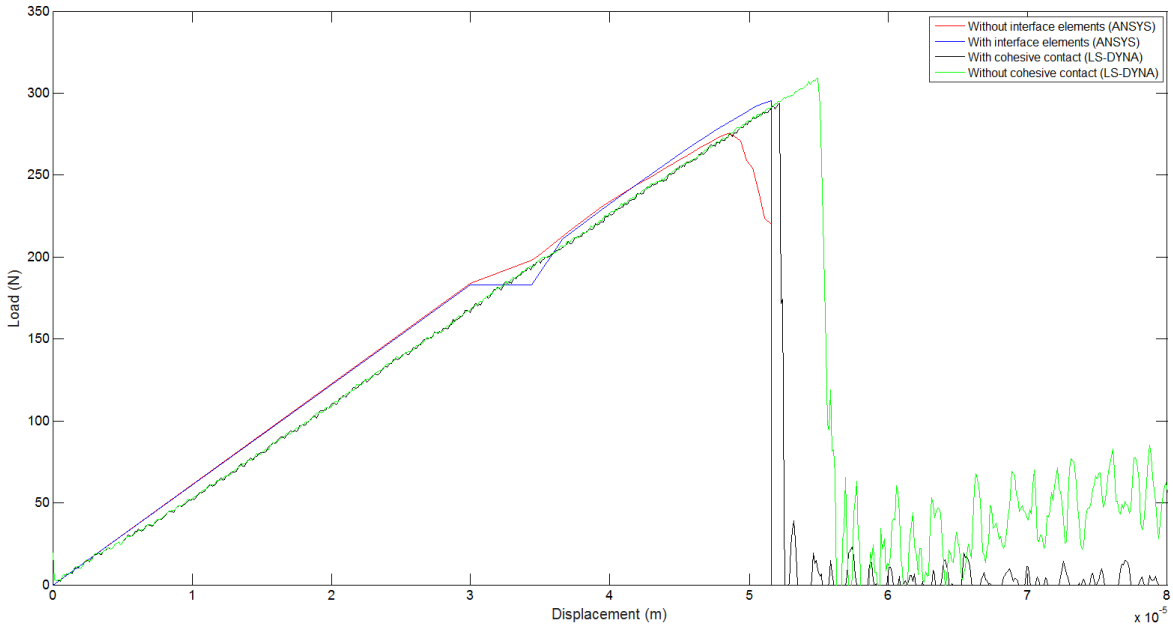


**Figure 4.10-** Comparison between the results obtained in LS-DYNA and ANSYS for the 15º/-75º numerical model

Observing the curves, the difference between the results of the models with and without cohesive properties and interface elements is around 1% and 11%, with Mangualde's models presenting a pick force of 297 N and 275 N for the model with and without cohesive interface elements, respectively. Both models, with and without cohesive properties, show a good correlation. As for the area where failure occurs in the elements, observing the results in Mangualde's dissertation [4], only the models without cohesive properties presented a different behavior. The area where the elements failed, observed in Figure 4.8, was not expected and visualizing the behavior of the test specimen in the tensile numerical test, this failure could have occurred due to one of the parameters in the model not being well adjusted. Further analysis should be made, in order to determine which parameter this is and, in consequence, obtain the expected results.

## 4.3 Numerical model of a test specimen with a 30°/-60° arrangement

In a similar manner as the one described above, Figure 4.11 represents the test specimen with a 30°/-60° arrangement. The boundary conditions, material properties, cohesive properties and sections are the same as the model with a 0°/90° arrangement.

After preparing the model, the simulation is carried out. Figure 4.12, Figure 4.13 and Figure 4.14 represent both final stages of the simulations with and without cohesive contact between the warp and weft, and the force-displacement curve for both simulations, respectively.

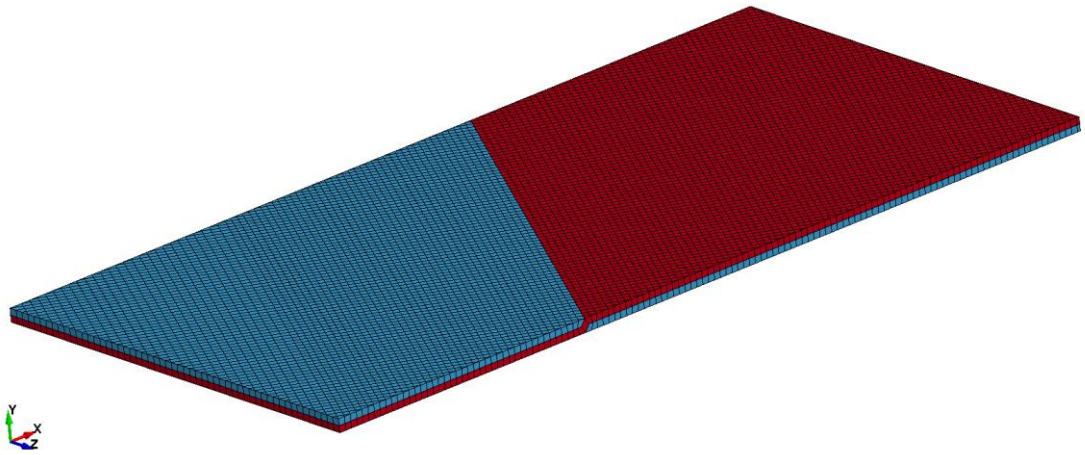

**Figure 4.11-** Test specimen with 30°/-60° arrangement

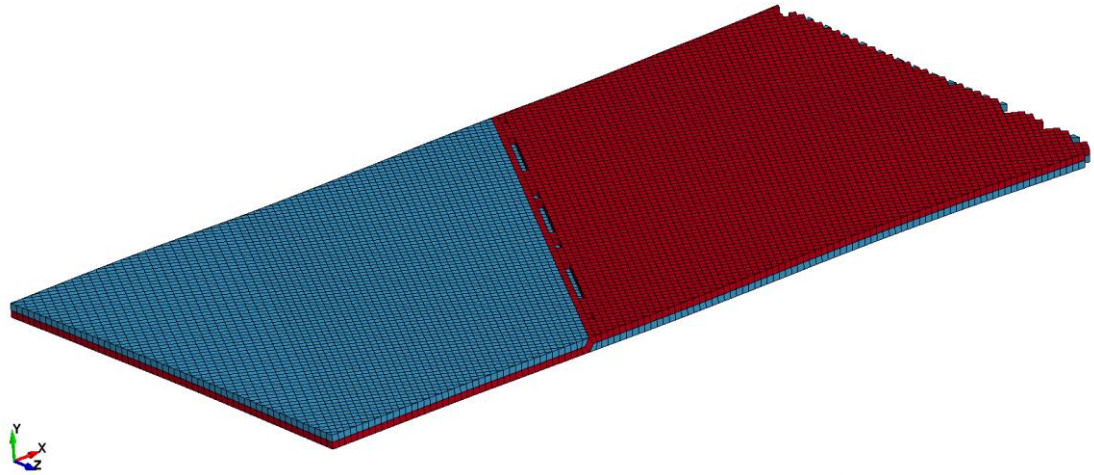

**Figure 4.12-** Final stage for the 30°/-60° test specimen with cohesive contact

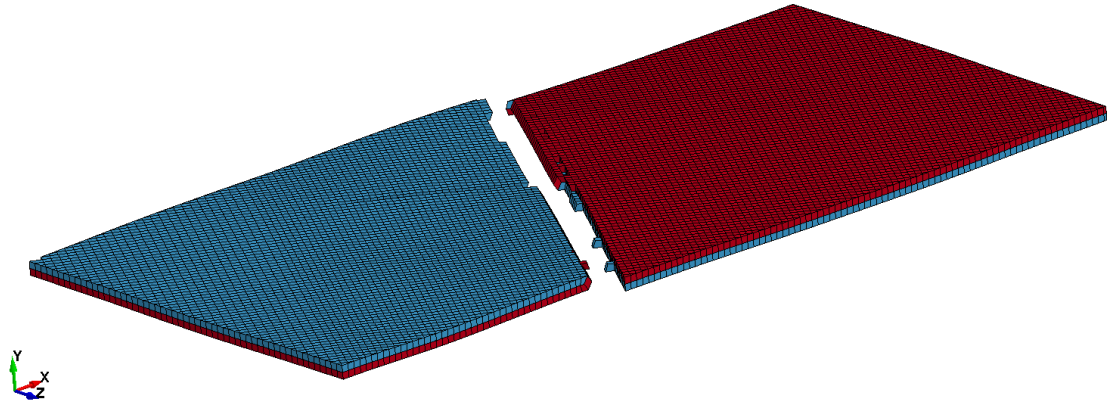

**Figure 4.13-** Final stage for the 30°/-60° test specimen without cohesive contact

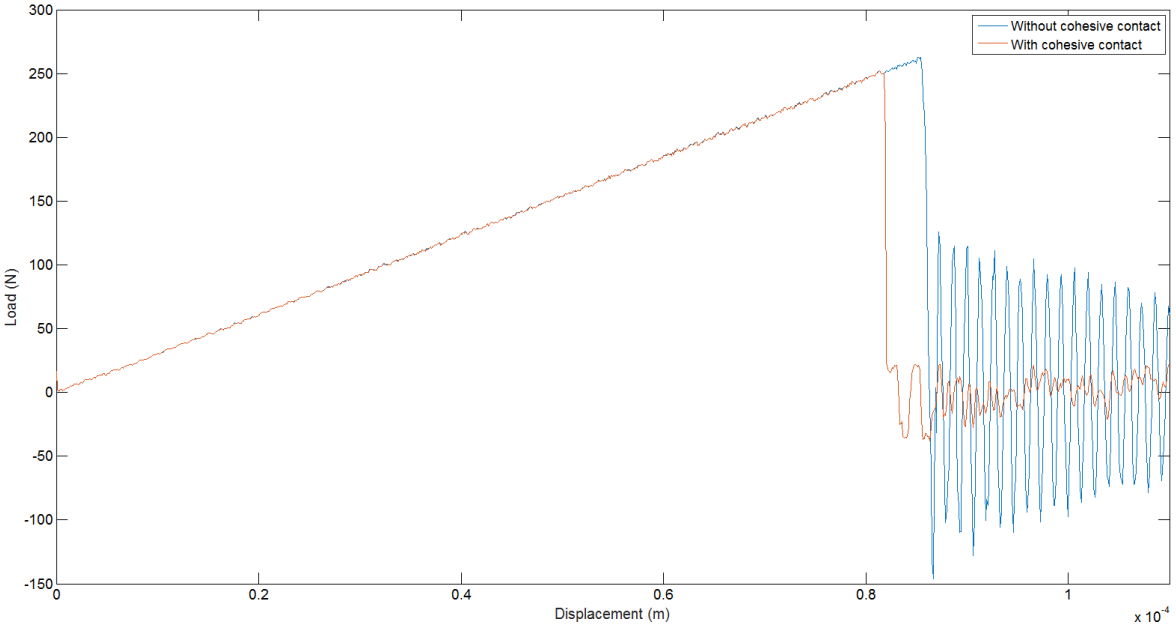


**Figure 4.14-** Comparison between the Force vs Displacement curves for both 30°/-60° models

Observing the final stages for both models, the behavior shown by the two models is in some way different, although not as different as in both models with a 15º/-75º arrangement. In the model where cohesive contact is implemented, element failure can be observed in the warp/weft transition, although the predominant failure occurs in the area where the displacement is imposed. As for the model without cohesive contact failure occurs in the area of the warp/weft transition, showing a "clean" cut in a similar way as the model with a 0°/90° arrangement.

As for the force-displacement curve, both simulations presented a similar maximum force right before failure occurred, with a maximum force of 252 N and 263 N, showing a difference of about 4%. As it was concluded in the last section, for this model, using cohesive contact between the warp and the weft does not affect significantly the load necessary to produce failure, however it affects the behavior of the ply when subjected to external forces.

In Figure 4.15 is depicted the comparison between the results obtained in LS-DYNA and the ones obtained by Mangualde in ANSYS.

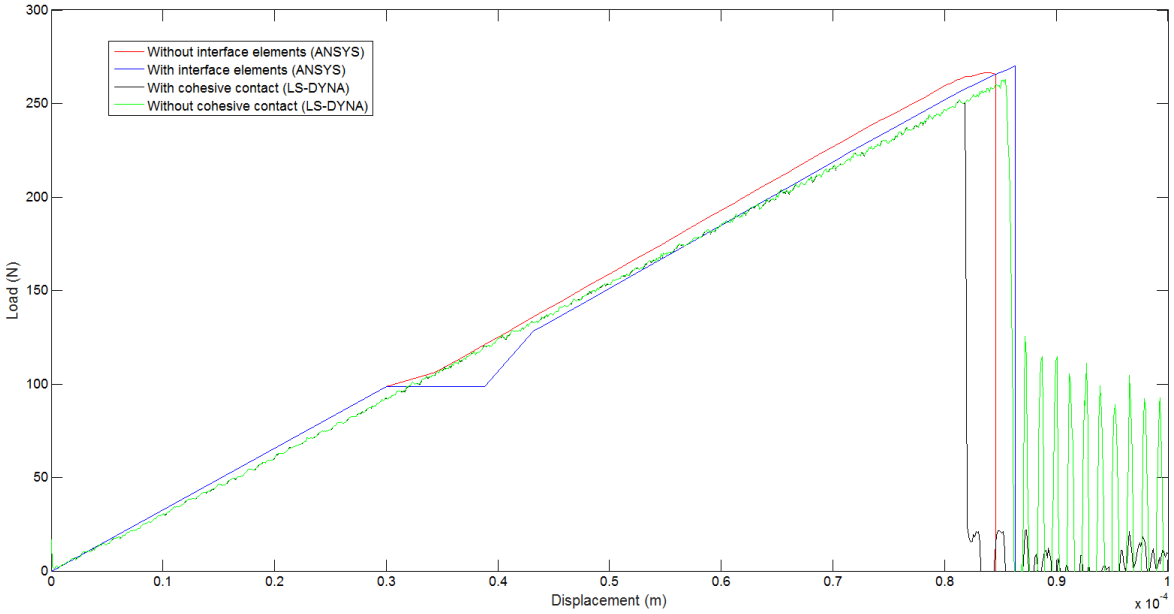


**Figure 4.15**- Comparison between the results obtained in LS-DYNA and ANSYS for the 30º/-60º numerical model

As depicted in Figure 4.15, Mangualde's models resulted in a maximum force of 270 N for the model with interface elements and 265 N for the model without. The difference between the results for the models with and without cohesive properties and interface elements is around 7% and 1.5%, respectively. Both models, with and without cohesive properties present a very good correlation, showing the best results so far. As for the area where failure occurs, observing the results in Mangualde's dissertation [4], only the models with cohesive properties presented a slightly different behavior, which could be explained with the same arguments presented in the last section. However, both results are not as different as the ones presented in the previous section, for some elements with a 30º arrangement failed near the warp/weft transition.

## 4.4 Numerical model of a test specimen constituted by 10 plies with a 0°/90° arrangement

In this chapter two test specimens constituted by 10 plies will be tested under tensile loads. As mentioned before, the position warp/weft transition for each ply is completely random, thus the model with cohesive contact between the warp and the weft and the model without present slightly different meshes, due to being generated in two different programs.

In Figure 4.16 is depicted the geometry of the test specimen and in Table 4.3 its dimensions are presented.

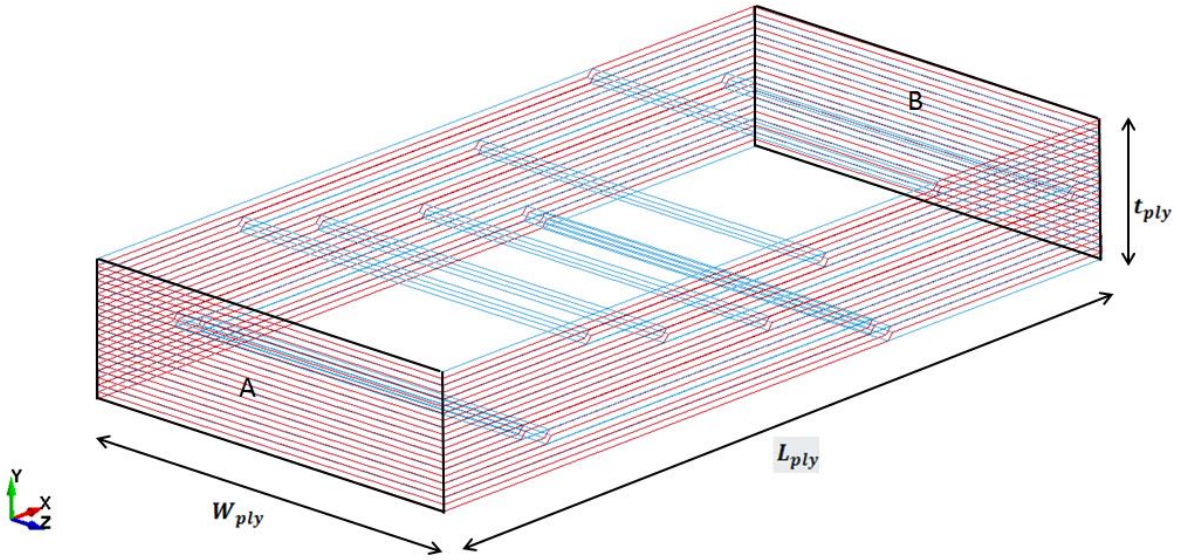


**Figure 4.16-** Representation of the test specimen constituted by 10 plies

**Table 4.3-** Dimensions of the test specimen of 10 plies

| $W_{ply}$ $(mm)$ | $L_{ply}$ $(mm)$ | $t_{ply}$ $(mm)$ |
|---|---|---|
| 10.05 | 20.01 | 3.3 |

The boundary conditions and the imposed displacement are the same as the previous models, i.e., a constraint in surface A and an imposed displacement of 0.11 mm in surface B, represented in Figure 4.16, both in the *x*-direction. The material properties of the plies, the cohesive elements and the cohesive properties of the contact between the warp and the weft are the same as in the model of one ply with a 0°/90° arrangement. However, for these models, the section of the solid elements constituting the plies is different. Given these models are constituted by ten plies instead of one, as a consequence the number of elements is much higher. This, accumulated with the element formulation -1 would implicate a very high computational cost. In order to prevent that from happening, element formulation 1 is implemented for the elements of the plies. An hourglass formulation 2 is also implemented in the model, in order to prevent nonphysical modes of deformation, given this element formulation is a constant stress solid element with one integration point.

After implementing all the features in the model, the simulation is carried out. Figure 4.17, Figure 4.18 and Figure 4.19 represent both final stages of the simulations with and without cohesive contact between the warp and weft and the force-displacement curve for both simulations, respectively.

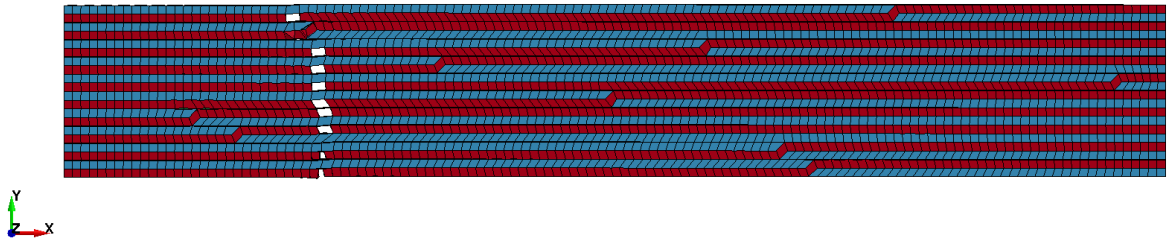


**Figure 4.17-** Final stage for the test specimen of 10 plies with cohesive contact

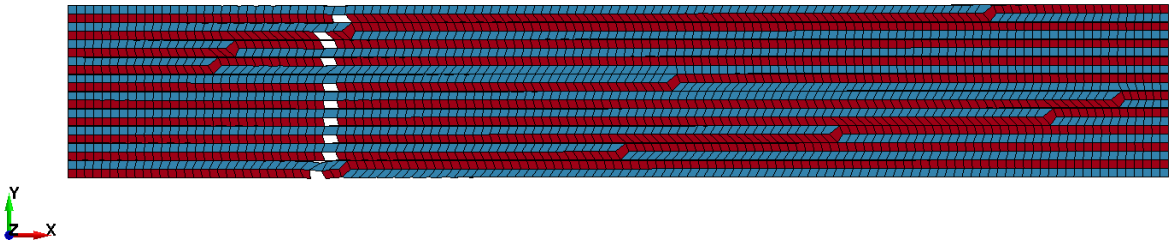


**Figure 4.18-** Final stage for the test specimen of 10 plies without cohesive contact

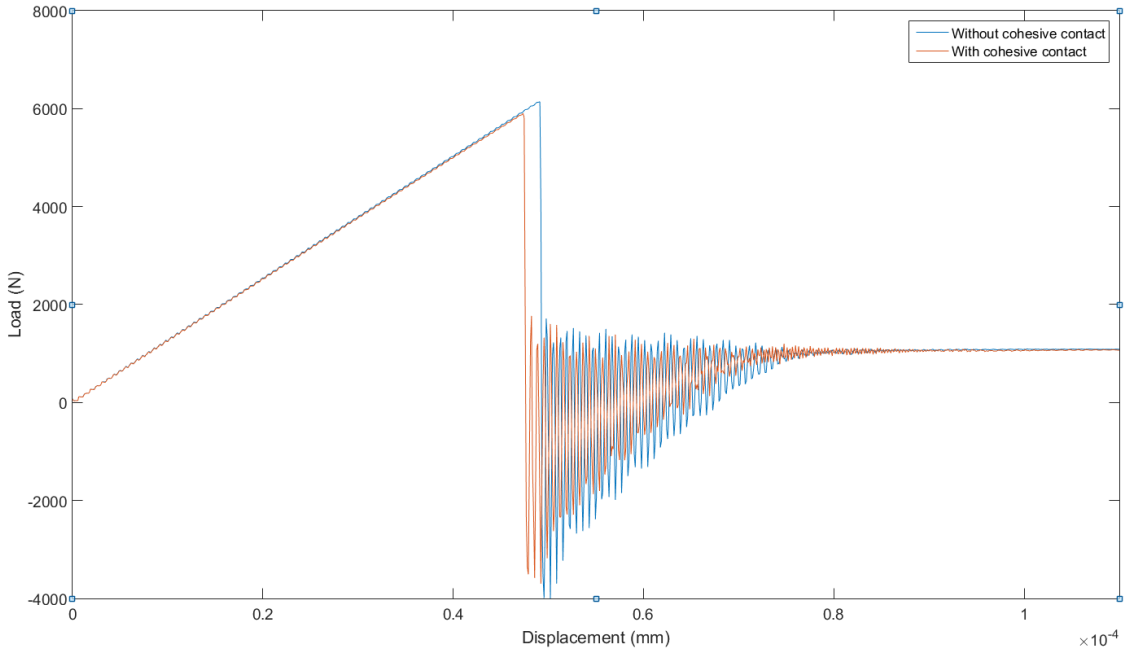


**Figure 4.19-** Comparison between the Force vs Displacement curves for both models of 10 plies

Although both models presented warp/weft transition for each ply at different locations, failure occurred in a very similar manner. For both models, as expected the solid elements that are oriented at 0° are the first to fail (fiber failure occurred first than matrix failure), which means that the elements failed by the maximum stress failure criteria. These fibers are aligned with the imposed displacement and, therefore, these are the ones that support much of the tensions present in the ply. After failure of these elements, some delamination is detected (failure of the cohesive elements, although not clearly visible in the respective figures) and the solid elements oriented at 90° (z-direction) showed no failure for the imposed displacement which means that, in order to observe a "clean" cut of the model, a higher displacement must be implemented.

Observing the force-displacement curve for both simulations, these showed very similar maximum forces right before failure occurred. Failure of the elements for the model with and without cohesive contact occurred at a force of about 5.90 kN and 6.15 kN, with a difference of about 4%.

As it was concluded for all the previous models, the implementation of cohesive contacts does not affect the behavior of the test specimen when subjected to external loads in relation to the force that is required in order to verify failure of the elements. However, for the area where these elements fail, only these models and the ones tested in chapter 4.1 show the same result.

## 4.5 Numerical model of a compression test specimen constituted by 26 plies with a 0°/90° arrangement

In this chapter a test specimen constituted by twenty-six plies is tested under compressive loads. Although Mangualde [4] was not able to study this model, the results will be compared with the ones obtained by Crespo [2]. Instead of simulating two models with and without cohesive contact, whose previous model results showed no direct influence to the load needed to cause failure, the influence of imposing a constrain in the *y*-direction to the top surface, to the stress strain results, will be studied. Crespo implemented this simplification to the model due to convergence issues. However, this constrain does not exist in the experimental tests. Figure 4.20 represents the geometry of the test specimen and in Table 4.4 the dimensions are presented.

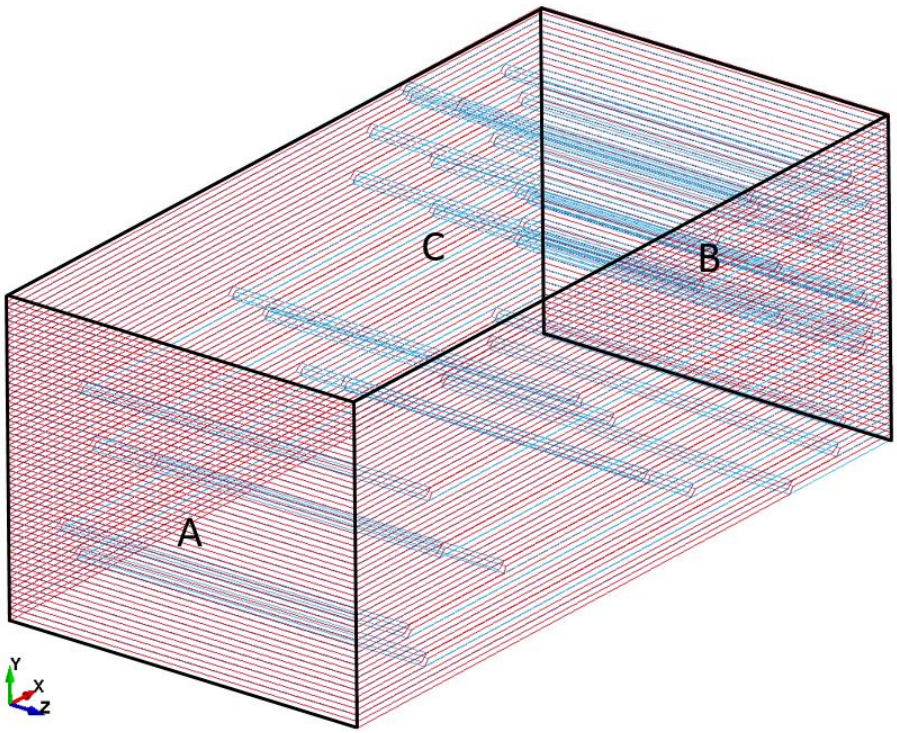


**Figure 4.20 -** Representation of the test specimen constituted by 26 plies

**Table 4.4 -** Dimensions of the test specimen of 26 plies

| $W_{ply}$ $(mm)$ | $L_{ply}$ $(mm)$ | $t_{ply}$ $(mm)$ |
|---|---|---|
| 10.05 | 20.01 | 8.164 |

The boundary conditions are a constraint in surface A, an imposed displacement of -0.22 mm in surface B, both in the *x*-direction, and, for one of the two models, a constrain in the *y*-direction in surface C. The properties of the material of the plies, the cohesive contact/elements, and the uniaxial test failure tensions constants that are used are altered and taken from Crespo's dissertation [2]. Crespo altered some of the properties and constants to achieve a higher failure result in the stress-strain curve. Table 4.5, Table 4.6 and Table 4.7 respectively represent the properties of the material of the plies, the cohesive contact/elements, and the uniaxial test failure tensions constants. The remaining conditions are the same as the ones implemented in the previous model.

**Table 4.5 -** Material properties of the plies

| $E_{11}$ $[GPa]$ | $E_{22}$ $[GPa]$ | $E_{33}$ $[GPa]$ | $\nu_{12}$ | $\nu_{23}$ | $\nu_{13}$ | $G_{12}$ $[MPa]$ | $G_{13}$ $[MPa]$ | $G_{23}$ $[MPa]$ |
|---|---|---|---|---|---|---|---|---|
| 62 | 4 | 4 | 0.32 | 0.32 | 0.436 | 5170 | 5170 | 3980 |

**Table 4.6 -** Properties of the cohesive contact/element

| **Contact** | ***MAT_138** | **Value** |
|---|---|---|
| NFLS | T $[MPa]$ | 30 |
| SFLS | S $[MPa]$ | 10 |
| PARAM | XMU | -1.5 |
| ERATEN | $G_{IC}$ $[N/mm]$ | 178.332 |
| ERATES | $G_{IIC}$ $[N/mm]$ | 970.851 |
| CT2CN | ET/EN | 1 |
| CN | EN $[N/mm^3]$ | $10^6$ |

**Table 4.7 –** Value of the failure tensions

| $X_T$ $[MPa]$ | $X_C$ $[MPa]$ | $Y_T$ $[MPa]$ | $Y_C$ $[MPa]$ | $S_L$ $[MPa]$ |
|---|---|---|---|---|
| 900 | 852 | 62.3 | 320 | 92.3 |

Given this is a compression test, in *MAT_ADD_EROSION instead of $X_T$, the variable SIGP1 is defined by $X_C$. After implementing all the features in the model, the simulation is carried out. Figure 4.21, Figure 4.22 and Figure 4.23 show both final stages of the simulations without and with the constrain and the stress-strain curves for the LS-DYNA model and ANSYS model, [2].

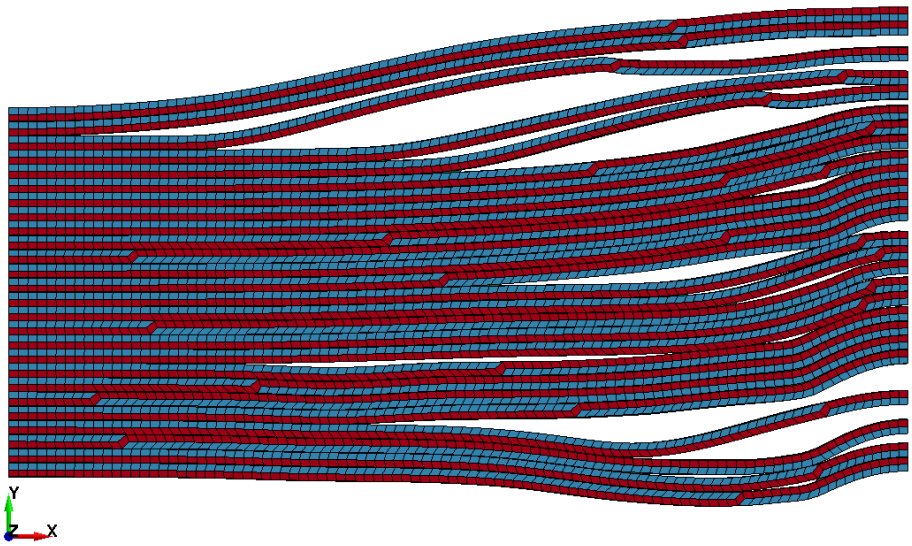


**Figure 4.21 -** Final stage for the test specimen of 26 plies without a constrain in the *y*-direction

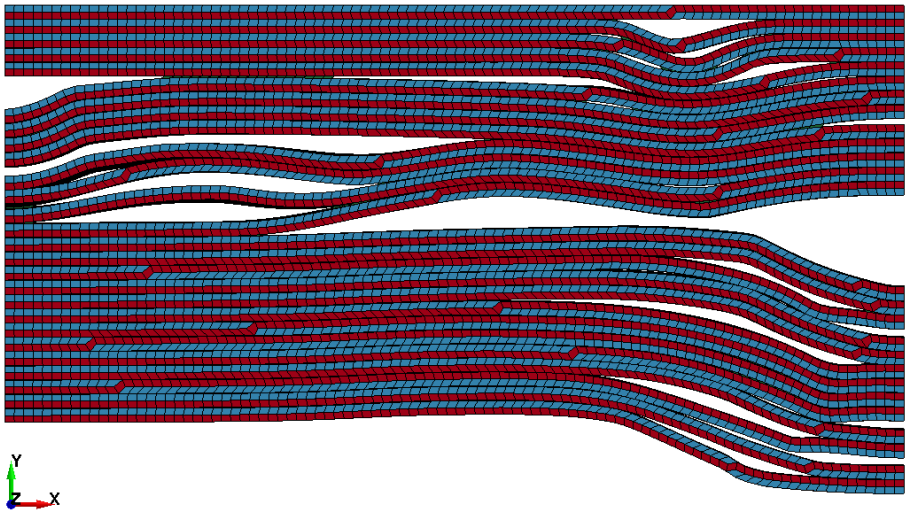


**Figure 4.22 -** Final stage for the test specimen of 26 plies with a constrain in the *y*-direction

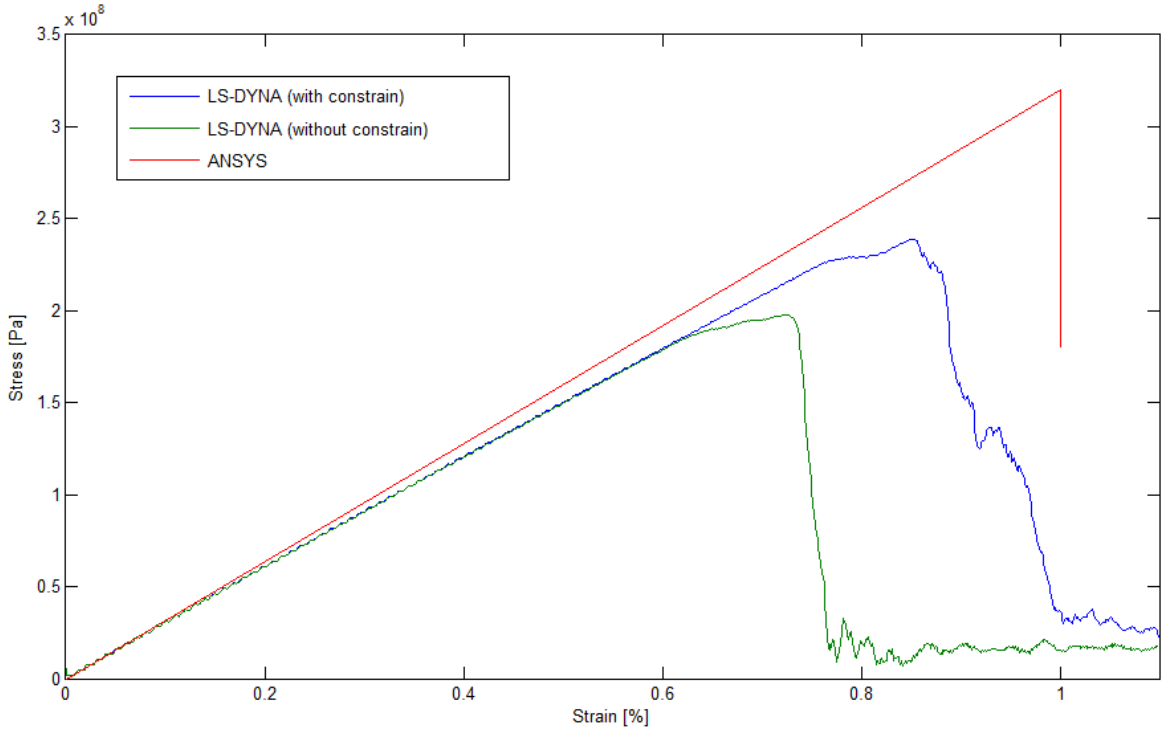


**Figure 4.23 -** Comparison of the Stress vs Strain curves for the LS-DYNA and ANSYS models of 26 plies

Observing both Figure 4.21 and Figure 4.22, the behavior was very similar and in both cases failure occurred due to delamination between the plies only and not between the warp and the weft. Also comparing the results with the ones obtained by Crespo [2] the behavior is not that different, although delamination is more present in the simulation ran in LS-DYNA. However, the stress-strain curves do not show results as good as the one obtained in the previous chapters. Observing Figure 4.23, the curve taken from the simulation ran in LS-DYNA, with a constrain in the *y*-direction, and Crespo's analysis show a difference of around 25% for the value of stress when failure occurs. This result might have to do with some of the inputs that are not well implemented in the model simulated in LS-DYNA or the model developed by Crespo having the same problem that Mangualde had in the beginning, which was not considering a local coordinate system for the transitional cells where the fibers direction has a rotation of approximately 45º. This last reason, if true, can affect the results of the area where the elements fail and/or the value of the stress/load to which the elements fail, as it can be observed in Mangualde's dissertation [4]. Finally, comparing both simulations ran in LS-DYNA, there is a difference around 20% and 15% for the stress and strain when failure occurs, respectively. It can be concluded that constraining the test specimen in the *y*-direction in that area affects the value for which the twenty-six plies will fail. However, more tests using both LS-DYNA and ANSYS/MATLAB must be conducted in order to determine which model is at fault and improve the model in order to replicate the results obtained in the experimental tests [2].

## 4.6 Conclusion Remarks

It was expected that implementing cohesive contact would not alter in a significant way the results when compared with the model without that contact, due to the warp and the weft sharing the same node at their interface, and the results proved it. Although in the tests of the plies with a 15°/75° and 30°/60° arrangement, failure of the elements occurred in different areas, all the other tests proved the models to behave in a very similar manner, with element failure in the same area (warp/weft transition). As for the force-displacement curves, both models for each of the four tests showed very similar maximum forces right before failure occurred at almost the same displacement value and, when comparing the curves obtained from the models with different arrangements, it is possible to determine that, as the fiber angle increases, the force and the displacement right before failure decreases and increases, respectively.

Also, while for the model with one ply with 0°/90° arrangement, element failure occurred in both elements oriented in different directions, in the model of ten plies, failure only occurs in the elements oriented at 0°.

Finally, the previous study demonstrated the influence of constraining the top surface in the *y*-direction and, to converge to the experimental results, more test must be done with this model.

All the models were simulated in a computer with an Intel ® Core ™ i7-5820k CPU@ 3.30 GHz processer and RAM 32Gb, using seven processing units. Table 4.8 shows the computational time for each simulation.

**Table 4.8 –** Computational time for each simulation

| | | |
|---|---|---|
| **1 ply 0º/90º** | With cohesive contact | 32 minutes 32 seconds |
| | Without cohesive contact | 25 minutes 14 seconds |
| **1 ply 15º/-75º** | With cohesive contact | 4 hours 6 minutes 14 seconds |
| | Without cohesive contact | 3 hours 25 minutes 26 seconds |
| **1 ply 30º/-60º** | With cohesive contact | 3 hours 21 minutes 31 seconds |
| | Without cohesive contact | 2 hours 15 minutes 45 seconds |
| **10 plies 0º/90º** | With cohesive contact | 3 hours 21 minutes 20 seconds |
| | Without cohesive contact | 2 hours 30 minutes 45 seconds |
| **26 plies 0º/90º** | With constrain in *y*-direction | 8 hours 25 minutes 24 seconds |
| | Without constrain in *y*-direction | 8 hours 10 minutes 30 seconds |

# 5
# Conclusion and Future Works

The main goal of this chapter is to summarize and describe the conclusions obtained from all the tests developed through this dissertation and their respective results.

This dissertation had its origin on the need to predict the behavior of composite materials in a less expensive and faster manner. Taking this into account, in order to predict failure and damage propagation in tensile and compressive tests, LS-DYNA finite element models are developed.

Given that this is the first contact with LS-DYNA, in order to fully develop the numerical model of a CFRP composite, tests, such as delamination and failure criteria were performed and presented in Chapter 3. Several tests for the delamination were conducted in order to determine the contact properties, the element formulation for the plies, the element type and the material properties for the cohesive elements that conducted to accurate results. In order to avoid interpenetration between the plies different eroding contact types can be implemented in the model, being selected the *Contact_Eroding_Single_Surface card. Regarding the element formulation, the research results showed that element formulation 5 for thick shell elements and 2 for solid elements presented the best results. As for the material, throughout extensive search, *MAT_138 showed to be the typical choice when using CZM models, being a material with a simple approach, when compared with other available materials models, and easy to implement. The results obtained with these two types of element formulation showed curves with a good correlation to the experimental results.

As for the failure criteria tests, the thick shell element type was excluded due to the material *MAT_ADD_EROSION not accepting the element formulation tested previously. A numerical model of one ply without cohesive elements was developed and subjected to tensile loads. Element formulation was, once more, modified to type -1, due to the model only having one element along the thickness. Results showed that the area with the higher stress concentration was in warp/weft transition. Failure was then observed near the area of the imposed displacement, which was not

expected, and for a maximum force with a difference around 2% from the one obtained by Mangualde, resulting in a validation of the implementation of the failure criteria.

After the validation of the implementation of cohesive properties and the combined failure criterion, six models of one ply with 0°/90°, 15°/75° and 30°/60° arrangements and two models for the ten plies and twenty-six plies test specimens with a 0°/90° arrangement (aiming the comparison of the test specimen's behavior when subjected to external loads) where tested, with all the features previously tested and described implemented. As results taken from the force-displacement curves show, both methods lead to very similar pick forces right before failure of the elements. As for the behavior, only the models of one ply with 15°/75° and 30°/60° arrangement show element failure occurring at a different area. Even if some parameters might need to be adjusted, results show a very good correlation with the ones obtained by Mangualde, leading to the validation of the developed models. As for the compressive test of the twenty-six plies, results show that constraining the top surface of the test specimen influences the stress necessary for element failure. Finally, when comparing with the data obtained by Crespo [2], a significant difference in the results can be observed, leading to the conclusion that more tests must be carried out in order to determine which model is at fault and converge the results with the experimental tests presented in Crespo's dissertation [2].

Most of the objectives imposed in the beginning of this dissertation were achieved. Thus analyzing the results, it can be concluded that the model with a 0°/90° arrangement (except for the twenty six plies) is presented as a good tool for predicting behavior and proving accurate results, while the other models, although validated and with results compliant with the expected ones, must first be tested taking into account the plasticity.

The models developed and respective features can be improved or further studied. In this section ideas and improvements will be suggested in order to improve the work that has been done so far.

- Implementation of user defined materials in order to simplify the use of the combined failure criteria and delamination;
- Validation of the model with 26 plies for all four arrangements;
- Implementation of plasticity for the models with a 15°/-75°, 30°/-60° and 45º/-45º arrangement;
- Use of optimization techniques, to adjust the parameters of the numerical model.

# References


[1] D. Miracle and S. Donaldson, “ASM Handbook”, 10th Editi. ASM International, The Materials Information Company, volume 21, 2001.

[2] I. Crespo, “Damage Propagation in Composite Materials Meso-Mechanical Models”, Master’s Thesis, Faculdade de Ciências e Tecnologia, Universidade Nova de Lisboa, 2015.

[3] LS-DYNA Theory Manual, March 2006.

[4] P. M. F. de S. P. Mangualde, “Numerical Analysis of CFRP of Mesoscale Models”, Master’s Thesis, Faculdade de Ciências e Tecnologia, Universidade Nova de Lisboa, 2016.

[5] R. F. Gibson, “Principles of Composite Material Mechanics,” Department of Mechnical Engineering,Way State University, McGraw-Hill, Inc, Detroit, Michigan, 1994.

[6] G. H. Staab, *LAMINAR COMPOSITES*, Butterworth-Heinemann; 1st edition, 1999.

[7] E. Music and A. Widroth, “Modelling of Spread Tow Carbon Fabric Composites for Advanced Lightweight Products”, Master’s thesis,Chalmers University of Technology, Goteborg, Sweden, 2013.

[8] P. Tan, L. Tong, and G. P. Steven, “Modelling for predicting the mechanical properties of textile composites -A review”, Composites Part A, volume 28, no. 1997, Sidney, Australia, 1997, pp. 903–922.

[9] “26-01-2016. URL:https://www.fose1.plymouth.ac.uk/sme/MATS347/MATS347C2%20fabrics.htm”.

[10] H. M. El-dessouky and C. A. Lawrence, “Ultra-lightweight carbon fibre / thermoplastic composite material using spread tow technology”, Composites: Part B, volume 50, 2013, pp. 91–97.

[11] “26-01-2016. URL: http://www.unmannedsystemstechnology.com/company/textreme/”.

[12] “26-01-2016. URL: http://www.turnology.com/?p=568928”.

[13] G. Milton, *The Theory of Composites*, Cambridge University Press; 1 edition, 2002.

[14] J.-M. Berthelot, *Composite Materials: Mechanical Behavior and Structural Analysis, Springer,* 1998.

[15] N. D. Cristescu, E. Craciun, and E. Soós, *Mechanics of Elastic Composites*, Chapman and Hall/CRC; 1st edition, 2003.

[16] Y. Kwon, D. H. Allen and R. R. Talreja, *Multiscale Modeling and Simulation of Composite Materials and Structures*, Springer, 2007.

[17] Y. Wan, B. Sun, and B. Gu, "Mechanics of Materials Multi-scale Structure Modeling of Damage Behaviors of 3D Orthogonal Woven Composite Materials Subject to Quasi-Static and High Strain Rate Compressions", Mechanics of Materials, volume 94, 2016, pp. 1–25.

[18] Weinan E, *Principles of Multiscale Modeling*, Cambridge University Press; 1st edition, 2011.

[19] O. Döbrich, T. Gereke, and C. Cherif, "Modeling the mechanical properties of textile-reinforced composites with a near micro-scale approach", Composite Structures, volume 135, 2016, pp. 1–7.

[20] C. Zhang, "Multi-Scale Characterization and Failure Modeling of Carbon/Epoxy Triaxially Braided Composite", PhD Thesis, Faculty of the University of Akron, 2013.

[21] V. Kozub, "Otimização robusta multiobjetivo de compósitos constituídos por polímero reforçado por fibra," Tese de Mestrado, Faculdade de Ciências e Tecnologia, Universidade Nova de Lisboa, 2016.

[22] A. Katunin, K. Dragan, and M. Dziendzikowski, "Damage identification in aircraft composite structures : A case study using various non-destructive testing techniques", Composite Structures, volume 127, 2015, pp. 1–9.

[23] P. M. Vert, "Modelizacion constitutiva y computacional del daño e la fractura de materiales compuestos", Thesis Doctoral, Universitat de Girona, 2006.

[24] V. W. Rosen, *Mechanics of composite strenghening*, Fibre Composite Materials, American Society of Materials, Metals Park, Ohio. 1965, pp. 37-75.

[25] R. Gutkin, S. T. Pinho, P. Robinson, and P. T. Curtis, "Mechanics of Materials A finite fracture mechanics formulation to predict fibre kinking and splitting in CFRP under combined longitudinal compression and in-plane shear", Mechanics of Materials, volume 43, 2011, pp. 730–739.

[26] A. Puck and H. Schurmann, "Failure Analysis of FRP Laminates by Means of Physical Based Phenomenological Models", Composites Science and Technology, volume 58, 1998, pp. 1045-1067.

[27] A. Puck, J. Kopp, and M. Knops, "Guidelines for the determination of the parameters in Puck ' s action plane strength criterion", Composites Science and Technology, volume. 62, 2002, pp. 371–378.

[28] P. P. Camanho, “Failure Criteria for Fiber-Reinforced Polymer”, Secção de Mecânica Aplicada, Departamento de Engenharia Mecânica e Gestão Industrial, Faculdade de Engenharia da Universidade do Porto, 2002, pp. 1–13.

[29] H. Zarei, *Experimental and Numerical Investigation of Crash Structures Using Aluminum Alloys*, Cuvillier Verlag Göttingen 2008.

[30] M. R. Karim, “Constitutive Modeling and Failure Criteria of Carbon Fiber’Reinforced Polymers Under High Strain Rates”, Master’s Thesis, University of Akron, 2005.

[31] P. G. Coelho, and J. B. Cardoso, “Apontamentos de Métodos Computacionais Em Engenharia Mecânica”, Departamento de Engenharia Mecânica e Industrial, Faculdade de Ciências e Tecnologia, Universidade Nova de Lisboa, p. 171, 2012.

[32] P. G. Coelho and J. B. Cardoso, “Integração Directa das Equações de Equilíbrio Dinâmico”, Departamento de Engenharia Mecânica e Industrial, Faculdade de Ciências e Tecnologia, Universidade Nova de Lisboa, p. 14, 2012.

[33] J. Jia, *Essentials of Applied Dynamic Analysis*. Springer, 2014.

[34] “13-08-2016. URL: http://www.dynasupport.com/howtos/element/hourglass.”.

[35] Simulia, *Abaqus 6.12: Getting started with Abaqus*, Interactive edition, 2012.

[36] S. T. Pinho, L. Iannucci, and P. Robinson, “Formulation and implementation of decohesion elements in an explicit finite element code”, Composites: Part A, volume 37, 2006, pp. 778–789.

[37] LS-DYNA Keyword User’s Manual, Volume II, Version 971, LSTC, May 2014.

[38] S. Marzi, L. Ramon-villalonga, M. Poklitar, and F. Kleiner, “Usage of Cohesive Elements in Crash Analysis of Large , Bonded Vehicle Structures - Experimental Tests and Simulation”, 2008.

[39] ANSYS Mechanical APDL Theory Reference, November 2013.

[40] P. P. Camanho and J. Costa, “An Engineering Solution for Mesh Size Effects in the Simulation of Delamination Using Cohesive Zone Models”, Engineering Fracture Mechanics, volume 74, 2007, pp. 1665–1682.

[41] K. Song, C. Dávila, and C. A. Rose, “Guidelines and Parameter Selection for the Simulation of Progressive Delamination”, NASA Langley Reasearch Center, 2008, pp. 1–15.

[42] S. A. Muflahi, G. Mohamed, and S. R. Hallett, “Investigation of Delamination Modeling Capabilities for Thin Composite Structures in LS-DYNA”, Advanced Composites Centre for Innovation and Science, 13th International LS-DYNA Users Conference 2014.

[43] LS-DYNA Keyword User's Manual, Volume I, Version 971, LSTC, August 2012.

[44] "22-07-2016. URL:http://www.dynasupport.com/tutorial/contact-modeling-in-ls-dyna/contact-types".

[45] W. P. Lin and H. Hu, "Nonlinear Analysis of Fiber-Reinforced Composite Laminates Subjected to Uniaxial Tensile Load", Jornal of Composite Materials, volume 36, no. 12, 2002, pp. 1429–1450.

[46] L. F. Kawashita, M. I. Jones, R. S. Trask, S. R. Hallett and M. R. Wisnom, " Static and Fatigue Delamination from Discontinuous Plies – Experimental and Numerical Investigations", CCM International Conferences on Composite Materials, 2009.

# Appendix

| Solid Element Formulation | Definition |
|---|---|
| **-2** | fully integrated S/R solid intended for elements with poor aspect ratio, accurate formulation |
| **-1** | fully integrated S/R solid intended for elements with poor aspect ratio, efficient formulation |
| **1** | constant stress solid element |
| **2** | fully integrated S/R solid |
| **19** | 4 point cohesive element |

| Thick-Shell Element Formulation | Definition |
|---|---|
| **2** | selective reduced 2 x 2 in plane integration |
| **5** | assumed strain reduced integration |

| Materials | Definition |
|---|---|
| ***MAT_002** | Valid material for modelling the elastic- orthotropic behavior of solids, shells and thick-shells |
| ***MAT_138** | This material includes a bilinear traction-separation law with quadratic mixed mode delamination criterion and a damage formulation |
| ***MAT_055** | This is an enhanced version of the composite model material type 22. Various types of failure can be specified following either the suggestions of Chang and Chang or Tsai and Wu |
| ***MAT_ADD_EROSION** | This option provides a way of including failure in models where failure and erosion is not allowed, although the option can also be applied to constitutive models with other failure/erosion criterion |